High-Coercivity Spin Glasses in Anisotropic Mo_2FeB_2-type $M_{1.5}Mn_{1.5}B_2$ (M = Mo, W)

Shola E. Adeniji[a], Alexei A. Belik[b], Takao Mori[b,c], Boniface P.T. Fokwa*[a]

[a] Department of Chemistry, University of California, Riverside, CA 92521, USA
[b] Research Center for Materials Nanoarchitectonics (MANA), National Institute for Materials Science (NIMS), Tsukuba 305-0044, Japan
[c] Graduate School of Pure and Applied Sciences, University of Tsukuba, Tsukuba 305-8577, Japan
*: E-mail: bfokwa@ucr.edu; www: fokwalab.ucr.edu

Abstract

Magnetic materials combining spin-glass behavior with hard-magnet coercivity are important for fundamental and applied research. Herein, we report spin glass behaviors coupled to remarkably large intrinsic coercivity values of 302.4 kA/m (H_c = 3.80 kOe) in $Mo_{1.5}Mn_{1.5}B_2$ and 175.1 kA/m (H_c = 2.20 kOe) in $W_{1.5}Mn_{1.5}B_2$. Both phases belong to the Mo_2FeB_2-type structure known for enabling excellent structural properties and predicted altermagnetic candidates. Single-phase products were obtained via a compositionally tuned solid-state route that resolves prior phase-purity challenges. Temperature-dependent susceptibility measurements revealed spin-glass behavior below the freezing temperatures T_g = 29 K for $Mo_{1.5}Mn_{1.5}B_2$ and T_g = 43 K (reentrant cluster spin glass) as well as a ferromagnetic (FM) transition at 70 K for $W_{1.5}Mn_{1.5}B_2$. AC susceptibility (χ') measurements exhibited frequency-dependent peaks that shifted to higher temperatures with increasing frequency, confirming the presence of dynamic spin freezing in both compounds. DFT calculations confirmed the presence of strongly competing FM and antiferromagnetic (AFM) interactions leading to competing AFM/FM/FiM orderings with a greater spin-exchange energy (ΔE_{ex} = 28–98 meV/f.u.) for FiM/AFM compared to FM in $Mo_{1.5}Mn_{1.5}B_2$ and even greater ΔE_{ex} = 53–131 meV/f.u. in $W_{1.5}Mn_{1.5}B_2$. The magnetocrystalline anisotropy energy (MAE) is uniaxial, favoring the *c*-axis, with MAE = −0.17 meV/f.u. (Mo) and −0.10 meV/f.u. (W), which align well with the large hysteresis found experimentally, while the unexpectedly larger coercivity of $Mo_{1.5}Mn_{1.5}B_2$ correlates with its greater ΔE_{ex}. These findings pave the way for designing new Mo_2FeB_2-type multifunctional materials beyond their usual structural materials characteristics.

Keywords: Mo_2FeB_2-type borides; spin glass; weak ferromagnet; uniaxial magnetic anisotropy, quantum materials

Introduction

Multifunctional materials are of great interest today because they combine multiple properties into a single material, delivering significant advantages across industries. Transition metal borides (TMBs) of the Mo_2FeB_2-type structure (space group *P4/mbm*) are multifunctional materials candidates. These are highly desired cermets widely studied for their excellent wear resistance, their low friction coefficients against non-ferrous metals, and their thermal expansion properties comparable to those of steels. [1–4] These attributes render them ideal for applications such as injection molding machine parts and tools as well as dies for copper extrusion [5]. Recent advancements in multicomponent boron-based materials have demonstrated their potential for property tuning by incorporating different atomic species into Mo_2FeB_2 structure type, enabling the development of materials with tailored characteristics for diverse industrial applications [6–12]. Also, theoretical predictions suggest that Mo_2MnB_2 exhibits better metallic properties with predominantly electron-like conductivity compared to Mo_2FeB_2;[13] and compounds such as Ta_2FeB_2, Mo_2MnB_2, Nb_2CrB_2, and Ti_2ReB_2 have been predicted to exhibit favorable thermodynamic and mechanical stability, with improved ductility relative to tungsten carbide (WC), a widely used wear-resistant material.[14] Additionally, Mn is a key component in impact- and wear-resistant alloys, making $Mo_2(Fe_{1-x}Mn_x)B_2$ solid solutions promising candidates for reinforcement phases in novel alloy designs. [15]

The presence of a magnetic element (Fe, Mn) in these compounds makes them candidates for magnetic properties research to achieve multifunctional properties by coupling their excellent mechanical strength with potential magnetic properties. Several computational studies have predicted antiferromagnetic (AFM) ordering for M_2FeB_2 (M = Mo, Nb, Ta). [5,16,17] In addition, recent studies reported a machine learning prediction of altermagnetic borides with Mo_2FeB_2 structure type. [18,19] However, such predictions have not yet been realized experimentally, mainly due to the difficulty encountered during their single-phase synthesis. Nevertheless, using a high-temperature (2000 K) and high-pressure (5.5 GPa) synthesis method, metastable Mo_2FeB_2 was obtained and partially (only the hysteresis was measured) demonstrated to order ferromagnetically,

[20] contrary to the previously predicted AFM ordering in the ground state structure of Mo_2FeB_2. The authors attributed this discrepancy to the metastable state of the high-pressure synthesized phase. Consequently, no experimental data is available on the ground state structure and on magnetic ordering in this exciting structure type. Our discovery of $M_{1.5}Mn_{1.5}B_2$ (M = Mo, W) phases aims to address both the synthesizability of Mo_2FeB_2-type compounds as well as their ground state magnetic properties. The presence of chains of magnetic elements (e.g. linear Fe-chains) in these structures render them interesting for studying quasi low-dimensional magnetic behaviors, including magnetic order, spin frustration and even spin-glass states. [11,21] Spin glasses are attracting considerable attention due to their ability to create unconventional magnetic behaviors (such as memory effects, slow dynamics, chaotic sensitivity, and reentrant transitions), [22–27] with applications in quantum computing envisioned. [28,29] Our work explores the possibility of achieving not only single-phase synthesis but also magnetic order or spin-glass state in Mo_2FeB_2-type TMBs by synthesizing M_2MnB_2 (M = Mo, W) along with the disordered variants, $M_{1.5}Mn_{1.5}B_2$ (M = Mo, W). The decision to adjust the stoichiometry stems from the premise that subtle variations in the M:Mn ratio can influence structural stability while modulating electronic and magnetic interactions within the boride framework. This compositional modification enables a more controlled synthesis process, offering valuable insights into the behavior of Mo_2FeB_2-type borides under varying experimental conditions. Additionally, increasing the Mn content will alter the magnetic properties of the systems, while non-stoichiometric compositions may induce spin-glass states. To complement our experimental efforts, we have undertaken density functional theory (DFT) studies to systematically evaluate structural stability, electronic properties, and magnetic characteristics.

Results and Discussion

Phase Formation, Purity Analysis and Crystal Structure Analysis

The synthesis of Mo_2MnB_2 and W_2MnB_2 resulted in mixed-phase products: MoB as a secondary phase in the case of Mo_2MnB_2 and unidentified peaks in the case of W_2MnB_2, as shown in **Figure S1**. These impurity-phases persisted despite attempts to optimize the synthesis conditions, including variation of the annealing temperature from 1000 °C to 1500 °C. In addition, our attempt to synthesize single phases using the arc melting method also failed. These findings suggest that

either the chosen synthesis routes are not adequate for obtaining single-phase products of these compounds, or the respective composition is not the ground state phase. To the best of our knowledge, all other reported synthesis methods of Mo_2FeB_2-type borides have failed to produce single-phase products. [4,15,30–35] Interestingly, the only report of a high-purity synthesis of Mo_2FeB_2-type borides was achieved under high-temperature (2000 K) and high-pressure (5.5 GPa) conditions, which led to the description of Mo_2FeB_2 as metastable. [20] We hypothesized that suppressing the formation of the MoB impurity during the synthesis of Mo_2MnB_2 would require a deviation from the ideal stoichiometry. To test our hypothesis, we targeted $Mo_{1.5}Mn_{1.5}B_2$ composition with the aim of reducing the Mo content while increasing Mn. Indeed, this adjustment led to the successful synthesis at 1220 °C of a single-phase product (**Figure 1a**) showing metallic luster. Using slightly modified experimental conditions such as a larger annealing temperature (1350 °C), single-phase $W_{1.5}Mn_{1.5}B_2$ was also synthesized (**Figure 1b**). The observed differences in phase formation between M_2MnB_2 and $M_{1.5}Mn_{1.5}B_2$ (M = Mo, W) indicate that this structure type might require a greater amount of 3d metals (T) in ternary M_2TB_2 phases than previously thought. Such compositional adjustments are not new in borides, for example the highly prolific $Ti_3Co_5B_2$ structure type [36] initially obtained from a 1:1:1 starting composition, was later demonstrated to be richer in Co ($Ti_{3-x}Co_{5+x}B_2$, x = 0–0.52) than initially reported, which was attributed to a Ti/Co mixed occupancy at one of the two Ti-sites in the structure [37]

Powder X-ray diffraction (PXRD) analysis (see **Tables 1** and **S1**) confirmed that M_2MnB_2 and $M_{1.5}Mn_{1.5}B_2$ (M = Mo, W) crystallize in the tetragonal crystal system, adopting the Mo_2FeB_2-type structure (space group *P4/mbm*, no.127). Rietveld refinements provided the refined lattice parameters (**Table S1**) that are larger than those previously reported; a = 5.8311(5) Å and c = 3.1487(3) Å (c/a = 0.540) for Mo_2MnB_2 and a = 5.790(2) Å and c = 3.1622(8) Å (c/a = 0.546) for W_2MnB_2 compared to a = 5.781–5.812 Å and c = 3.127–3.136 Å for M = Mo and a = 5.748 Å and c = 3.151–3.160 Å for M = W. [32,38] This discrepancy might also hint at a potential deviation from the ideal stoichiometry for these phases, especially given the relatively large ranges reported.

The lattice parameters of the Mn-richer phases (**Table 1**), a = 5.7897(1) Å and c = 3.1391(1) Å (c/a = 0.542) for $Mo_{1.5}Mn_{1.5}B_2$ and a = 5.7622(1) Å and c = 3.1604(1) Å (c/a = 0.548) for $W_{1.5}Mn_{1.5}B_2$, are smaller than those of the Mo/W-richer phases, as expected based on the smaller atomic radius of Mn versus Mo/W, supporting the increased Mn content. Interestingly, the c/a ratio

changes by only 0.006 between Mo- and W-based phases in Mn-poor or Mn-rich compositions (also found in DFT-calculated values given later), suggesting a maintained structural anisotropy despite variations in composition. Nevertheless, the small structural anisotropy is in favor of W-based compositions.

Rietveld refinements resulted in the atomic arrangements shown in **Figures 2(a–c)** illustrating different projections of the unit cell along the [001] and [010] crystallographic directions, while **Figure 2d** showcases the layered structure viewed along the [100] direction. The refinements of the Mn-richer compositions revealed that Mo (or W) and Mn atoms are mixed on the 4*h* Wyckoff site, while Mn exclusively resides at the 2*a* site (**Figure 2a**). This M:Mn site selectivity is primarily governed by electronic considerations rather than atomic size. Specifically, Mn, possessing a higher valence electron count (7 VE), preferentially occupies the 2*a* site because the greater number of valence electrons enables a higher coordination number with surrounding atoms. In these borides, a high electron count allows a metal center to stabilize more M–B and M–M bonds without forcing electrons into antibonding states. Electron-richer Mn (7 VE) can therefore support the more highly connected 2*a* environment (cuboctahedron, CN ≈ 12) by distributing its electrons over many bonds, whereas electron-poor Mo/W (6 VE) is better accommodated at the less connected 4*h* site (pentagonal prism, CN ≈ 10), where fewer bonds reduce the likelihood of antibonding occupation and allow stronger individual interactions. Thus, the match between electron count and site connectivity provides a straightforward rationale for the observed site preference. Conversely, Mo (or W) atoms, which have a smaller valence electron count (6 VE), predominantly occupy the lower coordination site (4*h*), but mixed with 25% Mn. The resulting coordination environment around Mn is a cuboctahedron (**Figure 3a**), while a pentagonal prism (**Figure 3b**) is formed around Mo (or W). This structural arrangement reinforces the stability of the boride framework, demonstrating how the electronic structure governs atomic site preference in these compounds.

SEM-EDS Analysis of $Mo_{1.5}Mn_{1.5}B_2$ and $W_{1.5}Mn_{1.5}B_2$

Given the impurity phases present in Mo_2MnB_2 and W_2MnB_2, further microstructural characterization focused primarily on the single phases $Mo_{1.5}Mn_{1.5}B_2$ and $W_{1.5}Mn_{1.5}B_2$. Scanning electron microscopy (SEM) revealed a homogeneous microstructure (**Figures 4a and 4b**) in both

materials, characterized by well-defined uniform spherical grey particles, suggesting controlled nucleation and growth.

Energy Dispersive X-ray Spectroscopy (EDS) mapping confirmed homogeneous distribution of the elements in both $Mo_{1.5}Mn_{1.5}B_2$ and $W_{1.5}Mn_{1.5}B_2$ (**Figures 4a and 4b**). Quantitative EDS analysis yielded an approximately 50:50 atomic ratio between Mo and Mn in $Mo_{1.5}Mn_{1.5}B_2$, and between W and Mn in $W_{1.5}Mn_{1.5}B_2$, which is consistent with their nominal stoichiometry. The minor variations observed in the measured compositions fall within the standard error range of EDS quantification. These results reinforce the successful synthesis of $Mo_{1.5}Mn_{1.5}B_2$ and $W_{1.5}Mn_{1.5}B_2$ as single-phase compounds with well-defined microstructure and homogeneous elemental distribution, providing a strong foundation for further investigation into their magnetic properties. Additional supporting data, including EDS spectra and compositional details, are provided as supplementary materials (**Figure S2**).

Experimental Magnetic Properties Investigations

The breakthrough in the single-phase synthesis of compounds ($Mo_{1.5}Mn_{1.5}B_2$ and $W_{1.5}Mn_{1.5}B_2$) adopting the Mo_2FeB_2-type structure marks a significant advancement in the study of their physical properties. The magnetic properties of $Mo_{1.5}Mn_{1.5}B_2$ and $W_{1.5}Mn_{1.5}B_2$ were investigated through temperature-dependent magnetization (*M*-*T*) measurements conducted at applied fields of 0.01 T and 0.1 T under both zero-field-cooled (ZFC) and field-cooled (FC) conditions. The resulting direct current (DC) magnetic susceptibility (χ) curves for ZFC and FC in $Mo_{1.5}Mn_{1.5}B_2$ exhibit spin-glass like behavior, as illustrated in **Figure 5a**. Notably, the ZFC curves show a typical AFM behavior, exhibiting a prominent peak around T_g = 29 K (freezing temperature, see AC susceptibility discussion below). Under the FC condition, $Mo_{1.5}Mn_{1.5}B_2$ transitions to FM-like behavior well below T_g (at ca. 14 K). At very low field (0.01 T), the susceptibility between ~150–250 K in **Figure 5a** shows a departure from ideal Curie–Weiss behavior, consistent with short-range magnetic correlations. Exchange disorder from Mo/Mn mixing and competing FM/FiM/AFM interactions can create locally correlated regions whose polarization varies nonlinearly with temperature in weak fields, yielding the observed curvature. Applying a stronger field (0.1 T) aligns spins more uniformly, reducing the deviation.

$W_{1.5}Mn_{1.5}B_2$ transitions to a FM-like behavior at T_C = 70 K under FC conditions (**Figure 5b**). Unlike $Mo_{1.5}Mn_{1.5}B_2$, which shows a single maximum under both magnetic fields, the maximum

observed in the ZFC conditions for $W_{1.5}Mn_{1.5}B_2$ varies with magnetic field, decreasing with increasing field from 43 K at 0.01 T to 21 K at 0.1 T. This behavior suggests that this W-phase might experience re-entrant spin-glass transitions below T_C. These behaviors indicate that there are competing AFM and FM interactions in both phases, but with dominating AFM interactions in $Mo_{1.5}Mn_{1.5}B_2$, while FM interactions prevail in $W_{1.5}Mn_{1.5}B_2$. A summary of the experimental magnetic parameters for both compounds is presented in **Table 2**. The origin of these different magnetic behaviors is further explored below, as well as through DFT calculations in the subsequent sections.

To deepen our understanding of these competitive magnetic interactions, the corrected inverse magnetic susceptibility (χ^{-1}) was plotted as shown in **Figures 5c and 5d**. At low applied magnetic fields, the curves do not follow the Curie-Weiss law, likely due to the competitive nature of the AFM and FM interactions. For reference, the low-field $\chi-1(T)$ data at 0.1 T under ZFC/FC conditions are shown in **Figure S3**, highlighting the deviation from linear Curie–Weiss behavior. Thus, measurements under a high magnetic field of 7 T were undertaken. Before fitting, we subtracted the temperature-independent term χ_0, which accounts for core diamagnetism and a small Van Vleck contribution. [39] For these high-field runs, the 7 T data were collected from 300–400 K under FC conditions. The $(\chi-\chi_0)^{-1}$ data in this range follow Curie–Weiss behavior and were fitted accordingly. The fits reveal a small and negative Weiss constant (θ = -15 K) for $Mo_{1.5}Mn_{1.5}B_2$, which indicates antiferromagnetic-dominated exchange on average; the low-temperature feature at Tg =29 K corresponds to spin freezing rather than long-range antiferromagnetic order. Conversely, $W_{1.5}Mn_{1.5}B_2$ exhibits a positive Weiss constant (θ = 77 K) close to Tc = 70 K, indicating the predominance of FM interactions. Overall, the Mo phase shows stronger magnetic competition than the W analogue. This frustration can originate from the spin-glass state, characterized by competing FM and AFM interactions.

To further investigate the possibility of spin-glass state, AC susceptibility measurements were performed to study the spin dynamics of $Mo_{1.5}Mn_{1.5}B_2$ and $W_{1.5}Mn_{1.5}B_2$. **Figures 6a and 6b** present the temperature-dependence of the real part (χ') of the AC susceptibility measured over a range of frequencies (2 Hz to 500 Hz) under a fixed AC magnetic field amplitude of 5 Oe. In both compounds, the $\chi'(T)$ curves exhibit well-defined peaks, the positions of which vary with frequency, a hallmark signature of spin-glass-like magnetic behavior. For $Mo_{1.5}Mn_{1.5}B_2$, a distinct

peak is observed around 28.5 K at the lowest frequency (2 Hz), which slightly shifts to a temperature of 29.5 K at the higher frequency (500 Hz). A different trend is noted for $W_{1.5}Mn_{1.5}B_2$, where a much broader maximum in χ' appears near 43 K at 2 Hz and moves to 45 K at 500 Hz as the frequency increases. This frequency dependence of the freezing temperature is a characteristic feature of systems undergoing a spin-glass transition, where spin relaxation dynamics are slow and thermally activated, leading to a time-dependent response. The relative variation of the peak temperature T_g in spin glasses per frequency f can typically be expressed using **Equation 1**

$$K = \Delta T_g / [T_g \Delta \ln f] \qquad \text{(Eq.1)}$$

where T_g is determined from the derivative of χ' with $d\chi'/dT = 0$, f is the frequency, and Δ points to the difference between measurements at different frequencies. We obtained K values of 0.00635 and 0.00842 for $M_{1.5}Mn_{1.5}B_2$ and $W_{1.5}Mn_{1.5}B_2$, respectively, which are relatively small for both systems and are indicative of the metallic nature of these compounds. [26]

One interesting point is that although the frequency dependence of $W_{1.5}Mn_{1.5}B_2$ is larger than $Mo_{1.5}Mn_{1.5}B_2$, there is a very large difference between the *Tg* of the DC measurement and the *Tg* of the AC measurements. The reason for this discrepancy is not clear, however, the peak is very broad in $W_{1.5}Mn_{1.5}B_2$. The peak in $Mo_{1.5}Mn_{1.5}B_2$ is sharper and more intense compared to that observed in $W_{1.5}Mn_{1.5}B_2$. This suggests a well-defined spin-glass transition in $Mo_{1.5}Mn_{1.5}B_2$, likely driven by dominating AFM interactions in the spin glass state, which is supported by the negative Weiss constant observed in the DC susceptibility analysis. $W_{1.5}Mn_{1.5}B_2$ is a little more anomalous, it exhibits a large positive Weiss constant θ = 77 K, namely strong FM interactions, while competition with weaker antiferromagnetic AFM interactions apparently leads to the spin glass ordering at a much lower temperature region. This complexity may result in the very broad DC peak and the anomalous difference with the AC peak temperatures. In addition, the AC data for $W_{1.5}Mn_{1.5}B_2$ at H_{dc} = 0 Oe (**Figure S4**) show a shoulder around 60 K next to the much stronger peak near 43 K (hiding the peak at 60 K from the ferromagnetic transition). The combination of a broad peak in $W_{1.5}Mn_{1.5}B_2$ and the presence of a peak at 60 K suggests a re-entrant spin-glass transition near 43 K.

To quantify the spin dynamics, we have analyzed the frequency dependence of T_{SG} in $W_{1.5}Mn_{1.5}B_2$, obtained under H_{DC} = 100 Oe, using the Power and Vogel–Fulcher scaling laws strategies

described by Roy-Chowdhury *et al.* [40,41] For the Power-law analysis, we used the expression in **Equation 2**,

$$\tau = \tau_0 \left[\frac{T_f - T_{SG}}{T_{SG}}\right]^{-zv} \qquad \text{(Eq. 2)}$$

where $\tau=1/(2\pi f)$ is the relaxation time at measurement frequency f, τ_0 is the microscopic attempt time, T_{SG} is the zero-field spin-glass temperature, and zv is the dynamical critical exponent. The Power law plot shown in **Figure 7a** is nearly linear and yields $\tau_0 = 1.2(3)\times10^{-13}$ s and $zv = 34.4(3)$ with T_{SG} =29.6 K (fixed), indicating slow collective dynamics characteristic of interacting moments. The Vogel–Fulcher analysis uses the expression in **Equation 3**,

$$\tau = \tau_0 \exp\left[\frac{E_a/k_B}{T_f - T_0}\right] \qquad \text{(Eq. 3)}$$

in which E_a is an activation energy, k_B is Boltzmann's constant, and T_0 is the interaction temperature. The fit shown in **Figure 7b** gives $\tau_0 = 1.4(9)\times10^{-13}$ s and E_a/k_B =269(9) K with T_0 =33.0 K (fixed), consistent with inter-cluster interactions producing an effective freezing barrier. To quantify the frequency shift of the χ' peak, we evaluated the Mydosh parameter Ω, defined in **Equation 4,**

$$\Omega = \frac{T_{f,2} - T_{f,1}}{T_{f,1}\,[\log_{10} f_2 - \log_{10} f_1]} \qquad \text{(Eq. 4)}$$

where T_f is the peak temperature at frequency f using our measured frequency window (2–500 Hz). We obtained Ω = 0.0208. This value lies in the cluster spin glass range (canonical spin glasses: Ω ≈ 0.005; cluster spin glasses: $0.01 \lesssim \Omega \lesssim 0.05$; superparamagnets: $\Omega \gtrsim 0.05$). In addition, we follow the optimized analysis in Roy-Chowdhury *et al.* [40] and analyze the E_a/k_BT_0 from the Vogel–Fulcher fit, which further separates canonical from cluster glasses (canonical: $E_a/k_BT_0 < 1$; cluster glass: >1). Together, Ω = 0.0208 and the scaling fits support the classification of our system as a cluster spin glass rather than a canonical spin glass

The field dependence of the freezing temperature at fixed frequency (110 Hz) was obtained from the χ'(T) maxima and fitted to an Almeida–Thouless (AT) form in **Equation 5**,

$$T_{SG}(H) = T_{SG}(0)\,(1 - AH^{2/\phi}) \qquad \text{(Eq. 5)}$$

where H is the applied DC field, $T_{SG}(0)$ is the zero-field value, A is a coefficient, and ϕ is the AT exponent. The fit yields ϕ = 5.2(4) and A = 0.025(5) as shown in **Figure 7c**, evidencing non-mean-

field for spin glasses. The obtained value of 5.2(4) for ϕ was observed in some Heisenberg spin-glass system. [41]

For $Mo_{1.5}Mn_{1.5}B_2$, the χ' peak shifts only slightly across our available frequency window (from $T_{SG} \approx 29.0$ K at 2 Hz to ≈ 29.5 K at 500 Hz), a change comparable to the temperature step in our measurements on the MPMS3. Because accurate application of the Power-law and Vogel–Fulcher analyses require T_{SG} values determined with finer resolution over a wider frequency span than available, we did not apply those fits here. This does not detract from the present conclusions: the AC data still show the expected low-frequency peak near 29 K, and the small frequency shift (together with the DC and coercivity results) is consistent with the spin-glass behavior established for this phase.

The magnetic behaviors of $Mo_{1.5}Mn_{1.5}B_2$ and $W_{1.5}Mn_{1.5}B_2$ were further investigated by field-dependent magnetization (*M-H*) measurements at temperatures between 5 K and 100 K, as shown in **Figures 8a and 8b.** At 5 K, the magnetization curve for $Mo_{1.5}Mn_{1.5}B_2$ exhibits a magnetic hysteresis loop and does not even trend toward saturation at high magnetic fields, indicating prominent spin glass behavior. Increasing the temperature reduces the coercivity and the magnetic moment but the overall shape remains until *T*g and the coercivity disappears completely thereafter suggesting that the paramagnetic state is reached. Conversely, at 5 K, the magnetization curve for $W_{1.5}Mn_{1.5}B_2$ also displays a magnetic hysteresis loop, but it shows a greater tendency towards magnetic saturation, further confirming dominating FM interactions. Similarly, with increasing temperature both the coercivity and the magnetic moment decrease, as expected, and a paramagnetic-like behavior (straight line) is found above T_C. Surprisingly, both *M-H* curves have very large coercivities at 5 K (**Figures 8c and 8d**) with values of 302 kA/m (*H*c = 3.8 kOe) and 175 kA/m (*H*c = 2.2 kOe) recorded for $Mo_{1.5}Mn_{1.5}B_2$ and $W_{1.5}Mn_{1.5}B_2$, respectively. Both $Mo_{1.5}Mn_{1.5}B_2$ and $W_{1.5}Mn_{1.5}B_2$ exhibit large H_c at low temperatures because of the following three combined effects of: (i) structural anisotropy arising from the tetragonal lattice; (ii) competing FM, FiM, and AFM interactions (see theory section below), which promote cooperative cluster reversal and stiffen the nucleation and motion of reversal fronts, consistent with the observed non-saturating M–H at 5 K; and (iii) Intrinsic uniaxial anisotropy (SOC-driven), supported by DFT MAE trends that lock the easy axis and increase the barrier to spin rotation (see theory section below). Microstructural strain and texture are known to influence coercivity: residual strain can

introduce domain-wall pinning centers (hardening), while strong texture can bias hysteresis by partially aligning easy axes. In our samples, the compositionally homogeneous microstructure and absence of obvious morphological texturing point to a minor microstructural contribution. The systematic increase in Hc therefore correlates more naturally with the intrinsic uniaxial anisotropy (MAE) as discussed below. The larger coercivity of $Mo_{1.5}Mn_{1.5}B_2$ relative to $W_{1.5}Mn_{1.5}B_2$ is unexpected, given that W is a heavier 5d element, which typically enhances anisotropy compared to 4d elements such as Mo. In $Mo_{1.5}Mn_{1.5}B_2$, the combined influence of stronger FM/FiM/AFM competition (see theory section below) and greater local anisotropy dispersion yields a higher effective reversal barrier than in $W_{1.5}Mn_{1.5}B_2$, despite W having a larger elemental spin–orbit constant than Mo; this accounts for the larger measured Hc of the Mo compound. The link between strong magnetic competition and elevated *H*c is consistent with prior observations in metal borides. In the $A_2MT_{5-x}T'_xB_2$ (A = Sc, Hf, Zr; M = Mn, Fe; T/T' = Rh, Ir; $Ti_3Co_5B_2$-type), compositions in which AFM interactions become more prominent tend to exhibit larger coercivities [42–44], a trend attributed to exchange-stiffened reversal and increased domain-wall hindrance in magnetically heterogeneous regions.

To the best of our knowledge, the recent study by Zhao et al. [45] is the only report of significant coercivity value in a metal boride exhibiting spin-glass behavior with a coercivity value of 10.2 kA/m (0.128 kOe) at 2 K reported in CrFeB, a value which is an order of magnitude smaller than those found in this work. We are not aware of other rare-earth-free metal borides with such larger intrinsic coercivity values. Given that such large coercivities are usually associated with hard magnetic materials, this discovery not only places these materials in the small group of materials candidates for spin-glass based spintronic applications,[28,29] but it also opens an avenue for developing rare-earth-free permanent magnetic materials based on the Mo_2FeB_2 structure type. Although these new materials are neither good ferromagnets nor strongly frustrated spin glasses, we argue that their position in-between these magnetic states benefits them greatly. Thus, novel quantum phenomena (e.g. useful in quantum computing) are highly likely to emerge from such systems. Indeed, Yamaraha et al [46] have recently shown that spin cluster glass materials (e.g. $Lu_3Fe_4Co_{0.5}Si_{0.5}O_{12}$) can provide high short-term memory capacity and are thus better candidates for constructing next-generation spintronic reservoir computing with improved performance if compared to conventional quantum material systems. Given that, a spin cluster glass behavior is

found in the W-phase, it is highly likely that this phase is also a potential candidate for constructing next-generation spintronic reservoir computing just like $Lu_3Fe_4Co_{0.5}Si_{0.5}O_{12}$.

Computational Analysis of Structure and Magnetic Properties

To complement the experimental magnetic properties of $Mo_{1.5}Mn_{1.5}B_2$ and $W_{1.5}Mn_{1.5}B_2$, we performed density functional theory (DFT) calculations. Several structural models, presented in **Figures S5 and S6**, were constructed to account for the mixed occupancies observed experimentally. We explored ferromagnetic (FM), antiferromagnetic (AFM), and ferrimagnetic (FiM) states (discussed later). Among the non-magnetic (NM) models, those with the lowest ground-state energies, depicted in **Figures S5A** (M = Mo) and **S6A** (M = W), were selected for further calculations. Given that all structure models have some kind of Mn_x-substructure not observed experimentally because of the M/Mn mixed occupancy, the lowest energy models were chosen for further calculations. These lowest energy structures feature an interesting Mn substructure: a chain of interconnected Mn_5 square pyramids (Mn_5-chain), illustrated in **Figures 9a** and **9b**. Although this substructure was not found experimentally, it is part of the network of interconnected Mn/M atoms (**Figure 2**). Interestingly, the Mn_5 unit exhibits two intrachain Mn–Mn bond lengths: a shorter one (2.60 Å in $Mo_{1.5}Mn_{1.5}B_2$; 2.62 Å in $W_{1.5}Mn_{1.5}B_2$), and a longer one (3.08 Å in $Mo_{1.5}Mn_{1.5}B_2$; 3.11 Å in $W_{1.5}Mn_{1.5}B_2$). The experimental Mn–T (T = Mo/W or Mn) bond lengths (2.65 Å/3.14 Å for $Mo_{1.5}Mn_{1.5}B_2$; 2.66 Å/3.16 Å for $W_{1.5}Mn_{1.5}B_2$) closely match calculated values, indicating that the proposed model structures are good enough to describe the experimental disordered ones. However, only the longer Mn–Mn distance (~3.15 Å) is found in M_2MnB_2, thus suggesting that vastly different magnetic interactions are expected between the Mn-poor and Mn-rich phases as demonstrated below.

The relaxation energy revealed that the spin-polarized (sp) calculations were energetically more favorable than the non-spin-polarized (nsp) ones in both compounds, indicating the presence of significant magnetic interactions. Further insights into their electronic structure and magnetism were obtained through density of states (DOS) analysis, as shown in **Figures 10a, 10b, 10e, and 10f**. In the nsp DOS plots, shown in **Figures 10a** and **10e**, Mn 3d states dominate the electronic structure near the Fermi level (E_F). Similarly, in the sp DOS, shown in **Figures 10b and 10f**, the overall shape and features are very similar in both compounds, particularly near the Fermi level, with only slight differences in the intensities between the spin-up and spin-down channels. This

suggests only minor differences between the two compounds, which is expected given that Mo and W have the same number of valence electrons, thus, the small differences originate from the different bonding characteristics between Mo 4d and W 5d orbitals in their respective environments. At E_F, the nsp-DOS is dominated by Mn d orbitals, and Mn states have the largest spin splitting in the sp-DOS, suggesting that Mn atoms are mostly responsible for the spin polarization and thus the magnetic properties in both compounds. Large states are still present at E_F, suggesting metallic behavior for both compounds, as expected from these metal-rich phases that showed metallic luster after synthesis.

More insight is gained by examining Mn–Mn bonding through pCOHP plots as presented in **Figures 10c and 10g**. In both compounds, the Fermi level lies within the Mn–Mn antibonding region in the nsp calculations, indicating electronic instability in the nonmagnetic state due to the occupation of antibonding states. Such occupation can lead to instability that is resolved not through atomic rearrangement, but via electronic structure distortion, specifically by differentiating spin sublattices to lower the system's energy through spin polarization. Thus, the Fermi level's position in the antibonding region signals a tendency toward spin symmetry breaking as a stabilization mechanism. This is supported by the spin-resolved pCOHP data, where Mn–Mn interactions are separated into α (spin-up) and β (spin-down) contributions as shown in **Figures 10d and 10h**. Upon spin polarization, both compounds show a reduction in antibonding character near the Fermi level, particularly in the α-spin Mn–Mn interactions. While the β-spin channel retains some antibonding character, the overall occupation of bonding states becomes more pronounced, especially between –1 eV and –5 eV. This redistribution of electronic states, with more electrons filling bonding orbitals and fewer occupying antibonding ones, reflects a strengthening of Mn–Mn bonds due to spin polarization. Such behavior is consistent with an electron-driven symmetry breaking, similar to a Jahn-Teller distortion, but here the instability is resolved purely through electronic reconfiguration.[47,48]

Although the sp pCOHP curves for the two compounds are similar in shape, subtle distinctions are observed. In $Mo_{1.5}Mn_{1.5}B_2$, both α and β Mn–Mn interactions exhibit relatively continuous bonding character below the Fermi level. In $W_{1.5}Mn_{1.5}B_2$, the α Mn–Mn bonding features appear slightly sharper, while the β component shows a somewhat more fragmented pattern. Nonetheless, these differences are not substantial, and the overall conclusion holds for both systems: spin

polarization reduces antibonding occupation at E_F and strengthens Mn–Mn bonding, thus stabilizing the overall structures. Non-spin polarized pCOHP can be used to predict magnetic interactions between magnetic centers such as Mn, with the presence of antibonding interactions at E_F of a nsp pCOHP plot suggestive of ferromagnetic (FM) interactions while nonbonding interactions point to antiferromagnetic (AFM) interactions.[47,48] Therefore, in both compounds, the strongly antibonding Mn-Mn interactions would predict strong FM interactions between magnetic Mn centers. However, the overall magnetic state of these compounds will depend upon the spin arrangements between the FM Mn-subunits (**Figure 9**) which are also affected by conduction electrons.

To gain deeper insights into the nature of magnetic state in $Mo_{1.5}Mn_{1.5}B_2$ and $W_{1.5}Mn_{1.5}B_2$, we explored multiple spin configurations using the ground state structure model. For each compound, three primary magnetic states FM, AFM, and ferrimagnetic (FiM) were analyzed, as illustrated in **Figures 11(a–d)**. For both compounds, the energy computed for the non-magnetic (NM) state is higher than that of the three magnetic states FM, AFM, and FiM, suggesting a high probability for magnetic ordering in both phases, the FM configuration being the most stable (**Table 3**). However, the NM state is only about 300 meV less stable than the FM ground state, which is far less than the usual values reported in other purely FM metal borides such as $MoMn_4SiB_2$ (about 1800 meV) or $Ti_3Co_5B_2$-type ferromagnets (about 1500-2000 meV). [12,21,39] However, in weak FM metal borides such as $Hf_2MOs_5B_2$ (M = Mn, Fe), [49] energy differences of the same order of magnitude are found (600-800 meV) and even a smaller value was found in $Hf_2CoOs_5B_2$ spin glass (94 meV).[49] Both these magnetic states (weak FM and spin glass) are characterized by competing FM and AFM interactions, just like our experimental results in the new phases. These findings suggest that the new phases contain the magnetic characteristics of either weak FM or spin glass states. To further probe the competition between FM and AFM interactions in the new phases, we have compared the energies of the FM, FiM and AFM states by analyzing the spin exchange energies relative to the most favorable FM state, defined as $E_{ex_1} = E_{FiM} - E_{FM}$, $E_{ex_2} = E_{AFM1} - E_{FM,}$ and $E_{ex_3} = E_{AFM2} - E_{FM}$ (see **Table 3**). For $Mo_{1.5}Mn_{1.5}B_2$, E_{ex_1} is +28 meV, while for $W_{1.5}Mn_{1.5}B_2$ it is twice as large at +53 meV, suggesting more competitive FM and AFM interactions in the Mo-based phase and greater FM interactions in the W-based phase. The AFM state is at least 60 meV higher in energy in both cases, given that E_{ex_2} (or E_{ex_3}) values are +90 meV (or 98 meV) and +131 meV (or +116 meV), for $Mo_{1.5}Mn_{1.5}B_2$ and $W_{1.5}Mn_{1.5}B_2$, respectively. Consequently, the

competitive AFM interactions originate mostly from a FiM state rather than an AFM state. Nevertheless, the AFM states are still competitive enough to make a significant contribution. These competing interactions corroborate the experimental results, which found a spin-glass state in $Mo_{1.5}Mn_{1.5}B_2$ and weak FM and re-entrant spin-glass states in $W_{1.5}Mn_{1.5}B_2$. The agreement between experimental and computational results suggests that both compounds exhibit competing magnetic interactions at low temperatures, likely driven by a complex interplay between localized and itinerant electronic states, a hallmark of spin glass behavior.

Magnetocrystalline Anisotropy Energy (MAE)

The MAE reflects the intrinsic energy barrier for changing the direction of magnetization in a crystal and it plays a crucial role in determining the coercivity of magnetic materials. In this study, we find that both $Mo_{1.5}Mn_{1.5}B_2$ and $W_{1.5}Mn_{1.5}B_2$ exhibit negative MAE values, with calculated values of –0.17 meV/f.u. and –0.10 meV/f.u., respectively, as presented in **Table 3**. According to the definition used in this work (see experimental section below), if MAE > 0, then E_{SOC} ($\perp$c) < E_{SOC} ($\parallel$c), so in-plane magnetization is energetically favored. Conversely, if MAE < 0, then E_{SOC} ($\parallel$c) > E_{SOC} ($\perp$c), indicating a preference for out-of-plane (easy axis) magnetization. Hence, the negative MAE values observed in both compounds indicate that the magnetic moments are more stable when aligned along the c-axis, suggesting that both materials possess uniaxial magnetic anisotropy. Notably, $Mo_{1.5}Mn_{1.5}B_2$ exhibits significantly higher MAE than $W_{1.5}Mn_{1.5}B_2$, a trend that aligns well with experimental findings of greater coercivity for $Mo_{1.5}Mn_{1.5}B_2$ (302.40 kA/m) compared to $W_{1.5}Mn_{1.5}B_2$ (175.07 kA/m). However, this result is somewhat counterintuitive because tungsten, a 5d transition metal, is expected to contribute more significantly to SOC-driven anisotropy than molybdenum, a 4d element. Therefore, one might anticipate $W_{1.5}Mn_{1.5}B_2$ to have both a larger MAE and higher coercivity than $Mo_{1.5}Mn_{1.5}B_2$. However, our results show the opposite situation, which invites a closer look into the underlying magnetic and electronic interactions. To explain this unusual behavior, we examined the magnetic exchange competition among the FM, AFM, and FiM states. As discussed earlier, the computed spin exchange energies relative to the FM ground state indicate that $Mo_{1.5}Mn_{1.5}B_2$ has closely competing AFM and FiM states, with energy differences of +92 meV/f.u. and +28 meV/f.u., respectively. This small energy separation indicates a more complex magnetic landscape and greater competition among magnetic orders. This pronounced FM/FiM/AFM competition implies that under an external magnetic field, spin clusters will reorient in a correlated manner rather than independently, which stiffens the

nucleation and motion of reversal fronts. When combined with the larger uniaxial MAE in $Mo_{1.5}Mn_{1.5}B_2$, the result is an increased effective field required to switch the magnetization, accounting for the higher measured *H*c of $Mo_{1.5}Mn_{1.5}B_2$ relative to $W_{1.5}Mn_{1.5}B_2$. However, both compounds still have huge coercivity values, which is a great advantage in achieving spintronic materials based on spin glass systems.

Conclusion

This study introduces $Mo_{1.5}Mn_{1.5}B_2$ and $W_{1.5}Mn_{1.5}B_2$ as single-phase Mo_2FeB_2-type borides exhibiting complex magnetic characteristics. Both compounds crystallize in the tetragonal *P*4*/mbm* space group and show clear site selectivity between Mo (or W) and Mn atoms. Magnetization measurements under varying temperatures reveal features of spin-glass behavior, and characteristic freezing temperature of T_g = 29 K for $Mo_{1.5}Mn_{1.5}B_2$ but two magnetic transitions for $W_{1.5}Mn_{1.5}B_2$, showcasing a ferromagnetic transition at 70 K and a re-entrant spin-glass transition around 43 K. Frequency-dependent AC magnetic susceptibility (χ') measurements show frequency-dependent shifts of the peak temperatures in both spin-glass states, validating the presence of dynamic spin freezing. In addition, field-dependent magnetization (*M*-*H*) measurements performed at 5 K reveal astonishingly large coercivity values for both compounds: *H*c = 302.40 kA/m for $Mo_{1.5}Mn_{1.5}B_2$ and *H*c = 175.07 kA/m for $W_{1.5}Mn_{1.5}B_2$. These intrinsic values are remarkably high for rare-earth-free borides. Density functional theory (DFT) calculations support these findings by revealing energetically competing FM, FiM, and AFM states, with stronger spin exchange competition in $Mo_{1.5}Mn_{1.5}B_2$. Furthermore, magnetocrystalline anisotropy energy (MAE) calculations show that both compounds prefer out-of-plane magnetization along the c-axis, supporting the large intrinsic coercivity values. The MAE of $Mo_{1.5}Mn_{1.5}B_2$ is nearly double that of $W_{1.5}Mn_{1.5}B_2$, which matches their coercivities. This exceptional magnetic performance marks a significant step in the discovery of new spin-glass-based spintronic materials and places Mo_2FeB_2-type borides firm in the multifunctional materials category beyond their usual structural materials characteristics.

Materials and Methodology

Synthesis

The syntheses of Mo_2MnB_2, W_2MnB_2, $Mo_{1.5}Mn_{1.5}B_2$, and $W_{1.5}Mn_{1.5}B_2$ were carried out using high purity elemental powders of tungsten (W, 99.9%, Across Organics), molybdenum (Mo, 99.9%, Thermo Scientific), manganese (Mn, 99%, Aldrich), and boron (B, 99%, amorphous powder, Thermo Scientific). The elements were precisely weighed to achieve the targeted stoichiometric ratios for each composition. Following the weighing process, the powders were thoroughly homogenized through grinding to promote uniform mixing. Using hydraulic press, the resulting powder mixtures were then compacted into dense pellets. These pellets were subsequently placed into dried and evacuated quartz ampoules, which were sealed under an argon atmosphere to prevent oxidation and unwanted contamination during high-temperature treatment.

To optimize the synthesis conditions, a modified solid-state reaction technique was employed, deviating from conventional methods used for Mo_2FeB_2-type borides. The ampoules were placed in a preheated box furnace at 1220 °C and annealed for 2 days to promote diffusion-driven reactions. After the heat treatment, the ampoules were rapidly quenched in cold water to stabilize the synthesized phases and suppress unwanted secondary phase formation. To further investigate the influence of synthesis temperature, additional trials were conducted by varying the annealing temperature between 1000 °C and 1500 °C, as well as using the arc furnace method. The resulting samples were examined for phase formation, microstructural homogeneity, and purity.

Phase Identification and Rietveld refinement

The phase purity and structural characterization of the synthesized samples were investigated using powder X-ray diffraction (PXRD). The finely ground powders were analyzed using a Rigaku Miniflex 600 diffractometer equipped with Cu-Kα_1 radiation (λ = 1.546 Å). Data acquisition was carried out in a continuous scan mode over a 2θ range of 5° to 90°, with a step size of 0.015°. To achieve high-resolution diffraction patterns with minimal noise, each scan was conducted over a duration of 2 hours. A Dectris MYTHEN2 1K detector was used to enhance signal detection and ensure precise peak resolution.

Structural analysis was performed using the Rietveld refinement method,[50] to determine the lattice parameters, phase composition, and crystallinity of the synthesized materials. The refinement process involved fitting experimental diffraction data to calculated patterns, enabling accurate determination of atomic positions and phase fractions. The obtained structural parameters were cross-validated against known a Mo_2FeB_2-type structure to confirm the successful synthesis of the

targeted compounds. This comprehensive approach ensured the reliability of phase identification and provided valuable insights into their structural properties.

Elemental Quantification and Imaging

Elemental composition and microstructural characterization were conducted using energy-dispersive X-ray (EDX) spectroscopy in conjunction with scanning electron microscopy (SEM). A Tescan Vega3 SBH SEM equipped with a Bruker LN_2-free high-resolution 30 mm^2 silicon drift (SD) detector was employed for the analysis. The EDX detector, with an energy resolution of ≤ 129 eV at Mn Kα, was calibrated using certified reference standards to ensure precise elemental quantification. The detection range extended from boron to californium, enabling a comprehensive assessment of both light and heavy elements. Multiple regions across the sample surface were examined to assess compositional uniformity, with quantitative data corrected using the ZAF algorithm to account for atomic number, absorption, and fluorescence effects. Additionally, backscattered electron (BSE) imaging was utilized to correlate microstructural features with elemental distributions. All measurements were conducted under high-vacuum conditions at an accelerating voltage of 20 kV and a working distance of 15 mm.

Magnetic Characterization

Magnetic behavior was analyzed using a Quantum Design MPMS3 SQUID magnetometer. Temperature-dependent DC magnetization measurements were carried out between 2 K and 400 K under both zero-field-cooled (ZFC) and field-cooled (FC) conditions at H = 0.01 T and 0.1 T to examine thermal evolution. Additionally, field-dependent DC magnetization curves were recorded at multiple temperatures to evaluate hysteresis characteristics and saturation tendencies. Temperature-dependent AC magnetization measurements were performed on cooling at H_{AC} = 5 Oe and H_{DC} = 0 and 100 Oe and frequencies between 2 and 500 Hz.

Computational Framework

The electronic and magnetic properties of M_2MnB_2 (M = Mo, W) and $M_{1.5}Mn_{1.5}B_2$ (M = Mo, W) systems were explored using computational simulations based on Density Functional Theory (DFT), implemented within the Vienna Ab-initio Simulation Package (VASP) [51,52]. The exchange-correlation interactions were treated using the generalized gradient approximation (GGA) with the Perdew-Burke-Ernzerhof (PBE) functional [53–55]. To accurately model the experimentally observed

Mo-site preference and site-sharing between Mo and Mn, and W and Mn where Mo and W preferentially occupies the 4*h* Wyckoff sites, a 1×1×2 supercell was constructed to statistically account for mixed occupancy.

The initial structures underwent full relaxation, allowing the lattice parameters, cell volume, and atomic positions to optimize until the forces on each atom were below 0.02 eV/Å. The projector augmented wave (PAW) method was employed to accurately treat the interaction between valence and core electrons. The Brillouin zone sampling was conducted using a Monkhorst-Pack [56] k-point mesh. A plane-wave cutoff energy of 550 eV was selected based on convergence tests to provide an adequate basis set quality. Total energy convergence was strictly enforced with a threshold of 10^{-6} eV per unit cell. Following structural relaxation, self-consistent calculations were performed to achieve electronic convergence and identify the most energetically favorable structures.

The Density of States (DOS) was subsequently computed using charge density data extracted from the CHGCAR file, with a grid resolution of 2000 points (NEDOS) to ensure high-resolution spectral features. The Fermi energy (E_F) was normalized to 0 eV for clarity in DOS visualizations. To analyze the magnetic behavior of these materials, both non-spin polarized (*nsp*), and spin-polarized (*sp*) calculations were conducted on the fully relaxed structures. This approach enabled a detailed investigation of the magnetic interactions and the stability of different spin configurations.

The projected crystal orbital Hamilton population (pCOHP) analysis was employed to evaluate the bonding interactions and electronic contributions to magnetic behavior. The pCOHP calculations were carried out using the LOBSTER (Local Orbital Basis Suite Towards Electronic-Structure Reconstruction) code [47,48], which reconstructs chemical bonding information by projecting the plane-wave outputs from VASP onto an atom-centered local orbital basis.

To evaluate the magnetocrystalline anisotropy energy (MAE), fully relativistic spin-orbit coupling (SOC) calculations were performed. The SOC effect arises from relativistic interactions between an electron's spin and its motion in the electric field of the atomic nucleus. This interaction is introduced through the SOC Hamiltonian [12], given by:

$H_{SOC} = \xi \mathbf{L} \cdot \mathbf{S}$ **(**Eq. 6)

where:

- H_{SOC} is the spin-orbit coupling Hamiltonian, which describes the additional energy contributions arising from the coupling between an electron's orbital and spin angular momenta
- ξ is the spin-orbit coupling constant, which is an atom-specific parameter reflecting the strength of relativistic interactions in the system.
- **L** is the orbital angular momentum operator.
- **S** is the spin angular momentum operator.
- **L.S** represents the interaction between the spin and orbital degrees of freedom of the electrons, which underlies the anisotropic magnetic behavior in crystalline solids.

In this context, SOC breaks the rotational symmetry of the spin system, giving rise to anisotropic total energies depending on the magnetization direction. This effect is responsible for magnetocrystalline anisotropy, an intrinsic property of magnetic materials.

To quantify this anisotropy, MAE is calculated using the total energies from SOC calculations with different magnetization orientations:

$$\text{MAE} = E_{SOC}(\parallel c) - E_{SOC}(\perp c) \quad \text{(Eq. 7)}$$

where:

- $E_{SOC}(\parallel c)$ is the total energy of the system when the magnetization is aligned parallel to the crystallographic *c*-axis.
- $E_{SOC}(\perp c)$ is the total energy when the magnetization lies in the plane perpendicular to the *c*-axis (typically within the *ab*-plane).

The MAE is defined as the energy difference between these two configurations and serves as a measure of the preferred spin orientation due to spin-orbit interactions.

Acknowledgements

BPTF acknowledges financial support from UC Riverside (CoR seed grant). TM acknowledges support from JST Mirai Program (JPMJMI19A1). We are grateful to the advanced computing and data resource program (ACCESS, funded by NSF) for allocations provided to support our DFT calculations at the San Diego Supercomputing Center.

References

(1) Takagi, K. High Tough Boride Base Cermets Produced by Reaction Sintering. *Mater Chem Phys* **2001**, *67* (1–3), 214–219. https://doi.org/10.1016/S0254-0584(00)00442-9.

(2) Yamasaki, Y.; Nishi, M.; Takagi, K. Development of Very High Strength Mo2NiB2 Complex Boride Base Hard Alloy. *J Solid State Chem* **2004**, *177* (2), 551–555. https://doi.org/10.1016/j.jssc.2003.03.008.

(3) Takagi, K. Development and Application of High Strength Ternary Boride Base Cermets. *J Solid State Chem* **2006**, *179* (9), 2809–2818. https://doi.org/10.1016/j.jssc.2006.01.023.

(4) Gladyshevskii, E. I.; Fedorov, T. F.; Kuz'ma, Yu. B.; Skolozdra, R. V. Isothermal Section of the Molbdenum-Iron-Boron System. *Soviet Powder Metallurgy and Metal Ceramics* **1966**, *5* (4), 305–309. https://doi.org/10.1007/BF00778631.

(5) Wang, B.; Liu, Y.; Ye, J.-W.; Wang, J. Electronic, Magnetic and Elastic Properties of Mo2FeB2: First-Principles Calculations. *Comput Mater Sci* **2013**, *70*, 133–139. https://doi.org/10.1016/j.commatsci.2012.12.023.

(6) Moraes, V.; Riedl, H.; Fuger, C.; Polcik, P.; Bolvardi, H.; Holec, D.; Mayrhofer, P. H. Ab Initio Inspired Design of Ternary Boride Thin Films. *Sci Rep* **2018**, *8* (1), 9288. https://doi.org/10.1038/s41598-018-27426-w.

(7) Wu, H.; Fan, H.; Hu, Y. Ab Initio Determination of Ultrahigh Thermal Conductivity in Ternary Compounds. *Phys Rev B* **2021**, *103* (4), L041203. https://doi.org/10.1103/PhysRevB.103.L041203.

(8) Ali, M. A.; Hossain, M. M.; Islam, A. K. M. A.; Naqib, S. H. Ternary Boride Hf3PB4: Insights into the Physical Properties of the Hardest Possible Boride MAX Phase. *J Alloys Compd* **2021**, *857*, 158264. https://doi.org/10.1016/j.jallcom.2020.158264.

(9) Sahoo, B. D.; Joshi, K. D. Novel Thorium Borides and Their Hardness and Superconductivity under Pressure: Ab Initio Calculations. *J Appl Phys* **2023**, *134* (6), 065903. https://doi.org/10.1063/5.0165402.

(10) Fokwa, B. P. T. Borides: Solid-State Chemistry. In *Encyclopedia of Inorganic and Bioinorganic Chemistry*; Wiley, 2014; pp 1–14. https://doi.org/10.1002/9781119951438.eibc0022.pub2.

(11) Shankhari, P.; Janka, O.; Pöttgen, R.; Fokwa, B. P. T. Rare-Earth-Free Magnets: Enhancing Magnetic Anisotropy and Spin Exchange Toward High-TC Hf2MIr5B2 (M = Mn, Fe). *J Am Chem Soc* **2021**, *143* (11), 4205–4212. https://doi.org/10.1021/jacs.0c10778.

(12) Adeniji, S. E.; Belik, A. A.; Mori, T.; Fokwa, B. P. T. Opening the Hysteresis Loop in MAB Magnets: Experimental and Computational Studies of CrMn4SiB2 and Mo0.8Mn4.2SiB2. *Chemistry of Materials* **2025**, *37* (6), 2349–2357. https://doi.org/10.1021/acs.chemmater.5c00187.

(13) Viswanathan, E.; Sundareswari, M.; Jayalakshmi, D. S.; Manjula, M. Fermi Surface and Hardness Enhancement Study on Ternary Scandium and Vanadium Based Borides by First Principles Investigation. *Comput Mater Sci* **2019**, *157*, 107–120. https://doi.org/10.1016/j.commatsci.2018.10.040.

(14) Onoprienko, A. A.; Ivashchenko, V. I.; Shevchenko, V. I. Structure and Properties of the Films Based on Ternary Transition Metal Borides: Theory and Experiment. *Condens Matter Phys* **2023**, *26* (2), 22701. https://doi.org/10.5488/CMP.26.22701.

(15) Prysyazhnyuk, P.; Di Tommaso, D. The Thermodynamic and Mechanical Properties of Earth-Abundant Metal Ternary Boride Mo2(Fe,Mn)B2 Solid Solutions for Impact- and Wear-Resistant Alloys. *Mater Adv* **2023**, *4* (17), 3822–3838. https://doi.org/10.1039/D3MA00313B.

(16) Touzani, R. St.; Fokwa, B. P. T. Electronic, Structural and Magnetic Studies of Niobium Borides of Group 8 Transition Metals, Nb2MB2 (M=Fe, Ru, Os) from First Principles Calculations. *J Solid State Chem* **2014**, *211*, 227–234. https://doi.org/10.1016/j.jssc.2013.10.013.

(17) Touzani, R. St.; Rehorn, C. W. G.; Fokwa, B. P. T. Influence of Chemical Bonding and Magnetism on Elastic Properties of the A2MB2 Borides (A=Nb, Ta; M=Fe, Ru, Os) from First-Principles Calculations. *Comput Mater Sci* **2015**, *104*, 52–59. https://doi.org/10.1016/j.commatsci.2015.03.036.

(18) Hou, X.-Y.; Yang, H.-C.; Liu, Z.-X.; Guo, P.-J.; Lu, Z.-Y. Large Intrinsic Anomalous Hall Effect in Both Nb2FeB2 and Ta2FeB2 with Collinear Antiferromagnetism. *Phys Rev B* **2023**, *107* (16), L161109. https://doi.org/10.1103/PhysRevB.107.L161109.

(19) Gao, Z.-F.; Qu, S.; Zeng, B.; Liu, Y.; Wen, J.-R.; Sun, H.; Guo, P.-J.; Lu, Z.-Y. AI-Accelerated Discovery of Altermagnetic Materials. *Natl Sci Rev* **2025**, *12* (4), nwaf066. https://doi.org/10.1093/nsr/nwaf066.

(20) Zhao, X.; Zhou, C.; Bao, K.; Zhu, P.; Ma, S.; Tao, Q.; Cui, T. Synthesis, Characterization, and First-Principles Analysis of the MAB-Like Ternary Transition-Metal Boride Fe(MoB)2. *Inorg Chem* **2022**, *61* (29), 11046–11056. https://doi.org/10.1021/acs.inorgchem.2c00635.

(21) Scheifers, J. P.; Zhang, Y.; Fokwa, B. P. T. Boron: Enabling Exciting Metal-Rich Structures and Magnetic Properties. *Acc Chem Res* **2017**, *50* (9), 2317–2325. https://doi.org/10.1021/acs.accounts.7b00268.

(22) Murphy, R. A.; Darago, L. E.; Ziebel, M. E.; Peterson, E. A.; Zaia, E. W.; Mara, M. W.; Lussier, D.; Velasquez, E. O.; Shuh, D. K.; Urban, J. J.; Neaton, J. B.; Long, J. R. Exchange Bias in a Layered Metal–Organic Topological Spin Glass. *ACS Cent Sci* **2021**, *7* (8), 1317–1326. https://doi.org/10.1021/acscentsci.1c00568.

(23) Krempaský, J.; Springholz, G.; D'Souza, S. W.; Caha, O.; Gmitra, M.; Ney, A.; Vaz, C. A. F.; Piamonteze, C.; Fanciulli, M.; Kriegner, D.; Krieger, J. A.; Prokscha, T.; Salman, Z.; Minár, J.; Dil, J. H. Efficient Magnetic Switching in a Correlated Spin Glass. *Nat Commun* **2023**, *14* (1), 6127. https://doi.org/10.1038/s41467-023-41718-4.

(24) Binder, K.; Young, A. P. Spin Glasses: Experimental Facts, Theoretical Concepts, and Open Questions. *Rev Mod Phys* **1986**, *58* (4), 801–976. https://doi.org/10.1103/RevModPhys.58.801.

(25) Yin, X.; Xu, C.; Lu, Q.; Li, J.; Feng, R.; Liu, F.; Liu, Z.; Zhang, B.; Chen, C.; Chen, L.; Huang, S.; Jiao, J.; Zhao, B.; Zhao, J.; Cao, Y.; Wang, G.; Ma, J.; Qian, D. Anisotropic Spin Glass Behavior of the Quasi-Two-Dimensional Buckled Honeycomb Compound Mg2Ni2Ta2O9. *Phys Rev B* **2024**, *110* (14), 144422. https://doi.org/10.1103/PhysRevB.110.144422.

(26) Mori, T.; Mamiya, H. Dynamical Properties of a Crystalline Rare-Earth Boron Cluster Spin-Glass System. *Phys Rev B* **2003**, *68* (21), 214422. https://doi.org/10.1103/PhysRevB.68.214422.

(27) Mori, T.; Leithe-Jasper, A. Spin Glass Behavior in Rhombohedral B12 Cluster Compounds. *Phys Rev B* **2002**, *66* (21), 214419. https://doi.org/10.1103/PhysRevB.66.214419.

(28) Brooke, J.; Bitko, D.; F., T.; Rosenbaum; Aeppli, G. Quantum Annealing of a Disordered Magnet. *Science (1979)* **1999**, *284* (5415), 779–781. https://doi.org/10.1126/science.284.5415.779.

(29) King, A. D.; Raymond, J.; Lanting, T.; Harris, R.; Zucca, A.; Altomare, F.; Berkley, A. J.; Boothby, K.; Ejtemaee, S.; Enderud, C.; Hoskinson, E.; Huang, S.; Ladizinsky, E.; MacDonald, A. J. R.; Marsden, G.; Molavi, R.; Oh, T.; Poulin-Lamarre, G.; Reis, M.; Rich, C.; Sato, Y.; Tsai, N.; Volkmann, M.; Whittaker, J. D.; Yao, J.; Sandvik, A. W.; Amin, M. H. Quantum Critical Dynamics in a 5,000-Qubit Programmable Spin Glass. *Nature* **2023**, *617* (7959), 61–66. https://doi.org/10.1038/s41586-023-05867-2.

(30) Carlsson, A.; Ronchi, R. M.; Rosen, J.; Dahlqvist, M. Computational Exploration of M-Sites with Chemical Order and Disorder in M′2M″B2 and M′4M″B3 Compounds. *Nanoscale* **2025**, *17* (6), 3478–3486. https://doi.org/10.1039/D4NR02948H.

(31) Sun, C.; Yu, H.; Liu, W. Microstructure, Mechanical Properties and First-Principles Calculations of Mo2FeB2-Based Cermets with Mn Addition. *Journal of the Ceramic Society of Japan* **2017**, *125* (9), 677–680. https://doi.org/10.2109/jcersj2.17113.

(32) V.S Telegus. Reaction of Groups VI and VII Transition Metals with Boron. *Khim. Khim. Tekhnol* **1970**, *1*, 96–100.

(33) Yu, H.; Zheng, Y.; Liu, W.; Zheng, J.; Xiong, W. Effect of Mn Content on the Microstructure and Mechanical Properties of Mo2FeB2 Based Cermets. *Int J Refract Metals Hard Mater* **2010**, *28* (2), 286–290. https://doi.org/10.1016/j.ijrmhm.2009.11.001.

(34) Yu, H.; Zheng, Y.; Liu, W.; Zheng, J.; Xiong, W. Effect of V Content on the Microstructure and Mechanical Properties of Mo2FeB2 Based Cermets. *Materials & Design (1980-2015)* **2010**, *31* (5), 2680–2683. https://doi.org/10.1016/j.matdes.2009.11.051.

(35) Yu, H.; Liu, W.; Zheng, Y. Effect of Carbon Content on the Microstructure and Mechanical Properties of Mo2FeB2 Based Cermets. *Int J Refract Metals Hard Mater* **2011**, *29* (6), 724–728. https://doi.org/10.1016/j.ijrmhm.2011.06.001.

(36) Kuz'ma, Yu. B.; Yarmolyuk, Ya. P. Crystal Structure of the Compound Ti3Co5B2. *Journal of Structural Chemistry* **1971**, *12* (3), 422–424. https://doi.org/10.1007/BF00744628.

(37) Shankhari, P.; Scheifers, J. P.; Hermus, M.; Yubuta, K.; Fokwa, B. P. T. Unexpected Trend Deviation in Isoelectronic Transition Metal Borides A3T5B2 (A = Group 4, T = Group 9): Ti3Co5B2- vs. Perovskite-Type Studied by Experiments and DFT Calculations. *Z Anorg Allg Chem* **2017**, *643* (21), 1551–1556. https://doi.org/10.1002/zaac.201700271.

(38) Telegus, V. S.; Kuz'ma, Yu. B. Phase Equilibria in the Systems Vanadium-Manganese-Boron, Molybdenum-Manganese-Boron, and Tungsten-Manganese-Bor On. *Soviet Powder Metallurgy and Metal Ceramics* **1971**, *10* (1), 52–56. https://doi.org/10.1007/BF00798049.

(39) Thota, S.; Ghosh, S.; R, M.; Joshi, D. C.; Medwal, R.; Rawat, R. S.; Seehra, M. S. Magnetic Ground State and Exchange Interactions in the Ising Chain Ferromagnet CoNb2O6. *Phys Rev B* **2021**, *103* (6), 064415. https://doi.org/10.1103/PhysRevB.103.064415.

(40) Roy-Chowdhury, M.; Seehra, M. S.; Thota, S. Optimized Analysis of the AC Magnetic Susceptibility Data in Several Spin-Glass Systems Using the Vogel–Fulcher and Power Laws. *AIP Adv* **2023**, *13* (11), 115020. https://doi.org/10.1063/5.0169800.

(41) Roy-Chowdhury, M.; Sarkar, T.; Weise, B.; Sang Choi, E.; Wen, Z.; Thota, S. Non-Equilibrium Spin Dynamics of the Frustrated Trication Spinel ZnMnCoO4 in the Hierarchical Free-Energy Framework. *Journal of Physics: Condensed Matter* **2025**, *37* (13), 135806. https://doi.org/10.1088/1361-648X/adb194.

(42) Luong, D.; Schumacher, L.; Kilic, S.; Haddon, E.; Pöttgen, R.; Fokwa, B. P. T. Enhancing Intrinsic Magnetic Hardness by Modulating Antagonistic Interactions in the Rare-Earth-Free Magnetic Solid Solution Hf2Fe1−δ Ru5−xIrx+δB2. *Chemistry – A European Journal* **2024**, *30* (13), e20230338. https://doi.org/10.1002/chem.202303381.

(43) Hermus, M.; Yang, M.; Grüner, D.; DiSalvo, F. J.; Fokwa, B. P. T. Drastic Change of Magnetic Interactions and Hysteresis through Site-Preferential Ru/Ir Substitution in Sc2FeRu5–XIrxB2. *Chemistry of Materials* **2014**, *26* (5), 1967–1974. https://doi.org/10.1021/cm500237h.

(44) Fokwa, B. P. T.; Lueken, H.; Dronskowski, R. Rational Design of Complex Borides – One-Electron-Step Evolution from Soft to Semi-Hard Itinerant Ferromagnets in the New Boride Series Ti2FeRu5–NRhnB2 ($1 \leq n \leq 5$). *Eur J Inorg Chem* **2011**, *2011* (26), 3926–3930. https://doi.org/10.1002/ejic.201100315.

(45) Zhao, X.; Bao, K.; Ma, S.; Zhou, C.; Zhu, P.; Tao, Q.; Cui, T. Revelation of the High Hardness and Spin Glass Behavior in the Novel Magnetic Material CrFeB. *J Alloys Compd* **2024**, *982*, 173800. https://doi.org/10.1016/j.jallcom.2024.173800.

(46) Liao, Z.; Yamahara, H.; Terao, K.; Ma, K.; Seki, M.; Tabata, H. Short-Term Memory Capacity Analysis of Lu3Fe4Co0.5Si0.5O12-Based Spin Cluster Glass towards Reservoir Computing. *Sci Rep* **2023**, *13* (1), 5260. https://doi.org/10.1038/s41598-023-32084-8.

(47) Dronskowski, R.; Bloechl, P. E. Crystal Orbital Hamilton Populations (COHP): Energy-Resolved Visualization of Chemical Bonding in Solids Based on Density-Functional Calculations. *J Phys Chem* **1993**, *97* (33), 8617–8624. https://doi.org/10.1021/j100135a014.

(48) Deringer, V. L.; Tchougréeff, A. L.; Dronskowski, R. Crystal Orbital Hamilton Population (COHP) Analysis As Projected from Plane-Wave Basis Sets. *J Phys Chem A* **2011**, *115* (21), 5461–5466. https://doi.org/10.1021/jp202489s.

(49) Gibson, K. A.; Luong, D.; Isaac, P. G.; Schumacher, L.; Pöttgen, R.; Fokwa, B. P. T. Computational and Experimental Investigations of Osmium-Rich Borides Hf2MOs5B2 (M = Mn, Fe, Co): From Spin Glass to Room-Temperature Magnetic Behaviors. *Inorg Chem* **2024**, *63* (17), 7869–7875. https://doi.org/10.1021/acs.inorgchem.4c00533.

(50) Rodriguez-Carvajal, J. FULLPROF: A Program for Rietveld Refinement and Pattern Matching Analysis. In *satellite meeting on powder diffraction of the XV congress of the IUCr*; Toulouse, France, 1990; Vol. 127.

(51) Kresse, G.; Joubert, D. From Ultrasoft Pseudopotentials to the Projector Augmented-Wave Method. *Phys Rev B* **1999**, *59* (3), 1758–1775. https://doi.org/10.1103/PhysRevB.59.1758.

(52) Hafner, J. Ab-initio Simulations of Materials Using VASP: Density-functional Theory and Beyond. *J Comput Chem* **2008**, *29* (13), 2044–2078. https://doi.org/10.1002/jcc.21057.

(53) Perdew, J. P.; Burke, K.; Ernzerhof, M. Generalized Gradient Approximation Made Simple. *Phys Rev Lett* **1996**, *77* (18), 3865–3868. https://doi.org/10.1103/PhysRevLett.77.3865.

(54) Blöchl, P. E. Projector Augmented-Wave Method. *Phys Rev B* **1994**, *50* (24), 17953–17979. https://doi.org/10.1103/PhysRevB.50.17953.

(55) Kresse, G.; Furthmüller, J. Efficient Iterative Schemes for Ab Initio Total-Energy Calculations Using a Plane-Wave Basis Set. *Phys Rev B* **1996**, *54* (16), 11169–11186. https://doi.org/10.1103/PhysRevB.54.11169.

(56) Monkhorst, H. J.; Pack, J. D. Special Points for Brillouin-Zone Integrations. *Phys Rev B* **1976**, *13* (12), 5188–5192. https://doi.org/10.1103/PhysRevB.13.5188.

Table 1. Structure refinement data for $Mo_{1.5}Mn_{1.5}B_2$ and $W_{1.5}Mn_{1.5}B_2$ based on PXRD data. Both compounds crystallize with the Mo_2MnB_2-type structure. Refined lattice parameters, unit cell volumes, densities, and Rietveld reliability factors are reported.

		$Mo_{1.5}Mn_{1.5}B_2$	**$W_{1.5}Mn_{1.5}B_2$**
Unit cell	Space group	*P*4/*mbm,* 127	*P*4/*mbm,* 127
dimension	$a = b$ (Å)	5.7897(1)	5.7622(1)
	c (Å)	3.1391(1)	3.1604(1)
	c/a	0.542	0.548
	V ($Å^3$)	105.25(1)	104.94(1)
	Density (g/cm^3)	7.826	12.02
Wykoff	2*a*	Mn: 0, 0, 0	Mn: 0, 0, 0
position	4*h*	75% Mo, 25% Mn: 0.1772(2), 0.6772(2), 0.5	75% W, 25% Mn: 0.1728(1), 0.6768(1), 0.5
	4g	B: 0.614(2), 0.114(2), 0	B: 0.631(2), 0.131(2), 0
Profile	R_{Bragg}	4.88	4.56
Refinement	R_f	3.67	2.92
(Rietveld)	χ^2	1.89	1.75

Table 2. Summary of key magnetic parameters for $Mo_{1.5}Mn_{1.5}B_2$ and $W_{1.5}Mn_{1.5}B_2$ compiled from DC susceptibility, high-field Curie–Weiss analysis, AC susceptibility, and low-temperature hysteresis measurements**.**

Parameter	**Symbol / Units**	**$Mo_{1.5}Mn_{1.5}B_2$**	**$W_{1.5}Mn_{1.5}B_2$**
Freezing temperature (under DC, ZFC)	T_g (K)	29	43
Curie temperature (under DC, FC)	T_c (K)	—	70
Weiss constant (7 T CW on $(\chi-\chi 0)^{-1}$	θ (K)	−15	+77
AC peak temperature (low f)	T_g (2 Hz) (K)	28.5	43.0
AC peak temperature (high f)	T_g (500 Hz) (K)	29.5	45.0
Frequency-shift	$K = \Delta T_g / [T_g \Delta \ln f]$ (dimensionless)	0.00635	0.00842
Coercivity at 5 K	Hc (kA·m^{-1})	302	175
Saturation tendency at 5 K	—	Non-saturating	Approaches saturation
Qualitative regime	—	Spin-glass-like / cluster-glass	FM with re-entrant glassiness

Table 3. Calculated magnetic moment (μ_A), spin-exchange energy (E_{ex}), and magnetocrystalline anisotropy energy (MAE) for $Mo_{1.5}Mn_{1.5}B_2$ and $W_{1.5}Mn_{1.5}B_2$ across various magnetic configurations: ferromagnetic (FM), ferrimagnetic (FiM), antiferromagnetic (AFM1 and AFM2), and nonmagnetic (NM). The spin-exchange energy is defined relative to the FM state (ground state set to $E_{FM} = 0$ meV/f.u.): $E_{ex_1} = E_{FiM} - E_{FM}$; $E_{ex_2} = E_{AFM1} - E_{FM}$; $E_{ex_3} = E_{AFM2} - E_{FM}$; $E_{ex_4} = E_{NM} - E_{FM}$.

Compound	**Total magnetic moment (μ_A)**		**Spin-exchange energy**				**Magnetocrystalline anisotropy energy**
	μ_A (FM) μ_B/f.u.	μ_A (FiM) μ_B/f.u.	E_{ex_1} meV/f.u.	E_{ex_2} meV/f.u.	E_{ex_3} meV/f.u.	E_{ex_4} meV/f.u.	MAE meV/f.u.
$Mo_{1.5}Mn_{1.5}B_2$	2.76	1.72	+28	+92	+98	+307	-0.17
$W_{1.5}Mn_{1.5}B_2$	2.55	1.70	+53	+131	+116	+309	-0.10

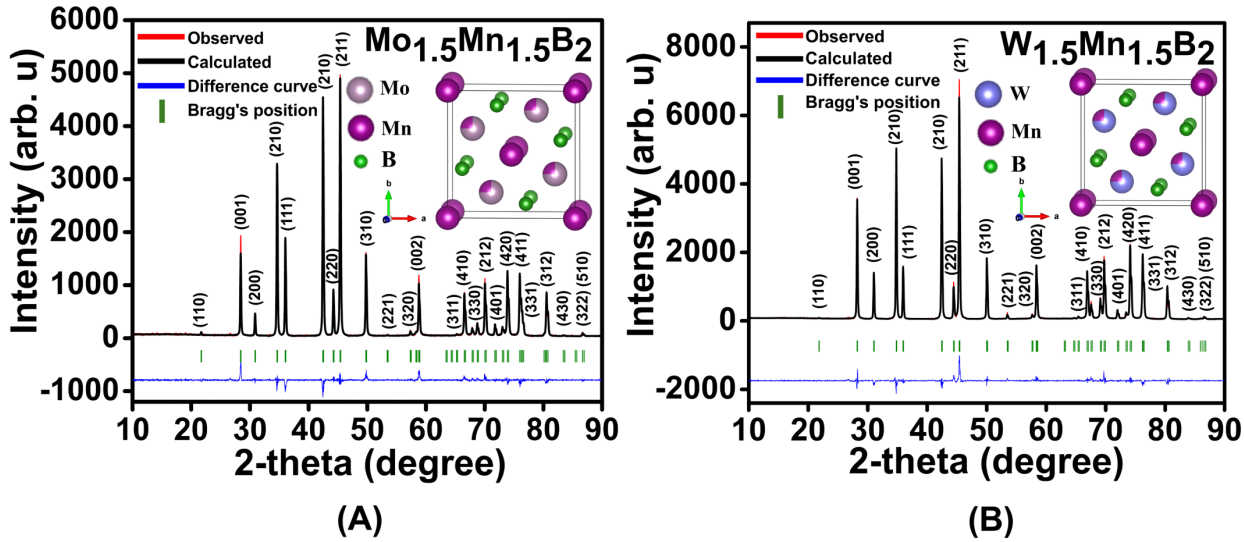


Figure 1. Rietveld refinements of the powder X-ray diffraction patterns (Cu $K\alpha_1$; λ = 1.5406 Å) for $Mo_{1.5}Mn_{1.5}B_2$ (A) and $W_{1.5}Mn_{1.5}B_2$ (B). Red, black, and blue curves correspond to the observed, calculated, and difference profiles, respectively, with green vertical ticks indicating Bragg reflection positions. The two diffractograms are similar (same structure type), but subtle differences in intensities are apparent with some small reflections even disappearing in one compared to the other. Insets display the refined unit cells.

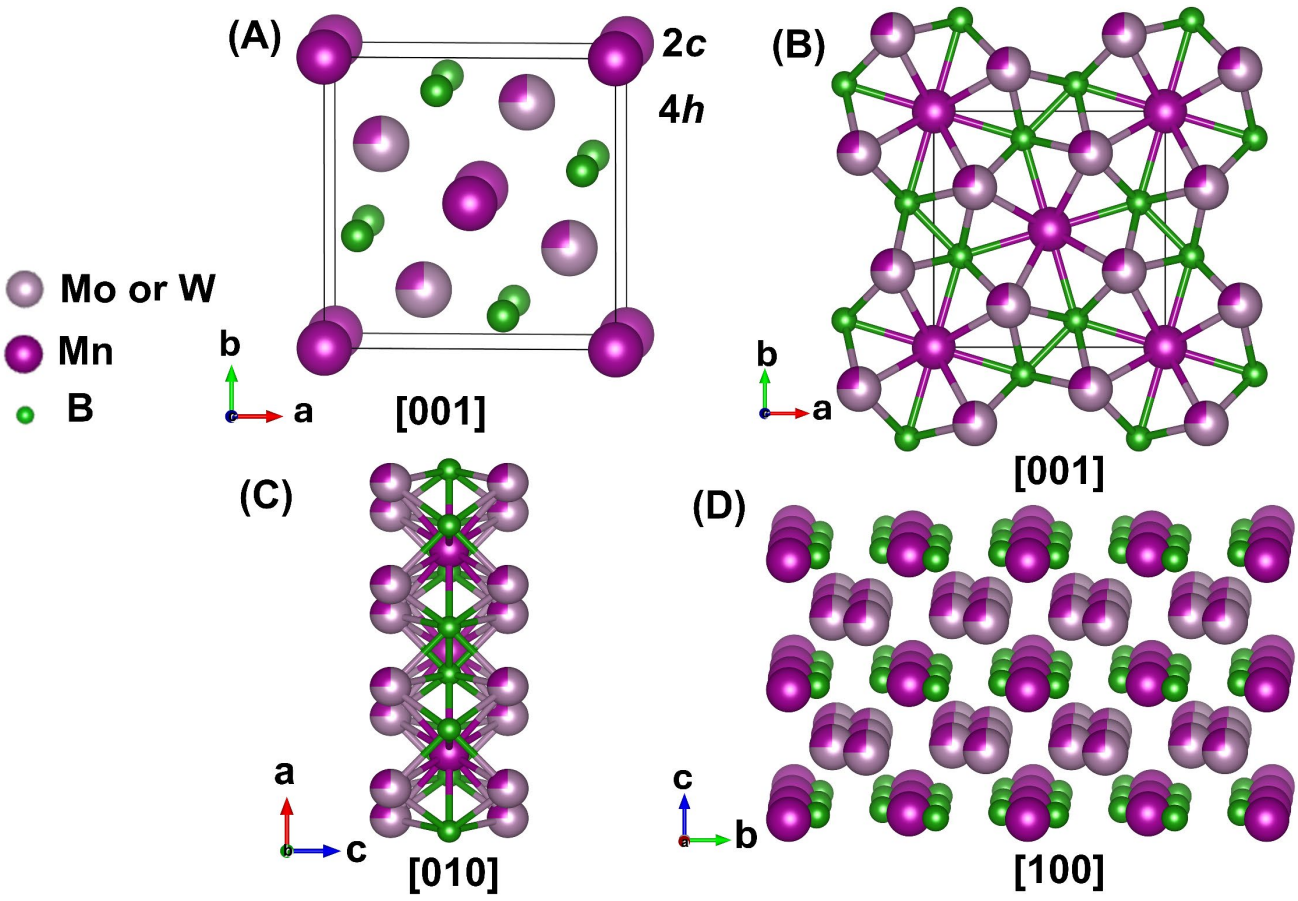


Figure 2. (A) Crystal structure of $M_{1.5}Mn_{1.5}B_2$ (M = Mo, W) viewed along the [001] direction, highlighting Wyckoff positions responsible for M (4*h*) and Mn (2*c*) site preferences. (B) and (C) Atomic arrangements along the [010] and [001] directions, respectively. (D) Three-dimensional layer-like structure viewed along the [100] direction, emphasizing the alternating stacking of the magnetic 3d transition metal (Mn) and boron in one layer and mostly 4d transition metal (75%M + 25%Mn) in another.

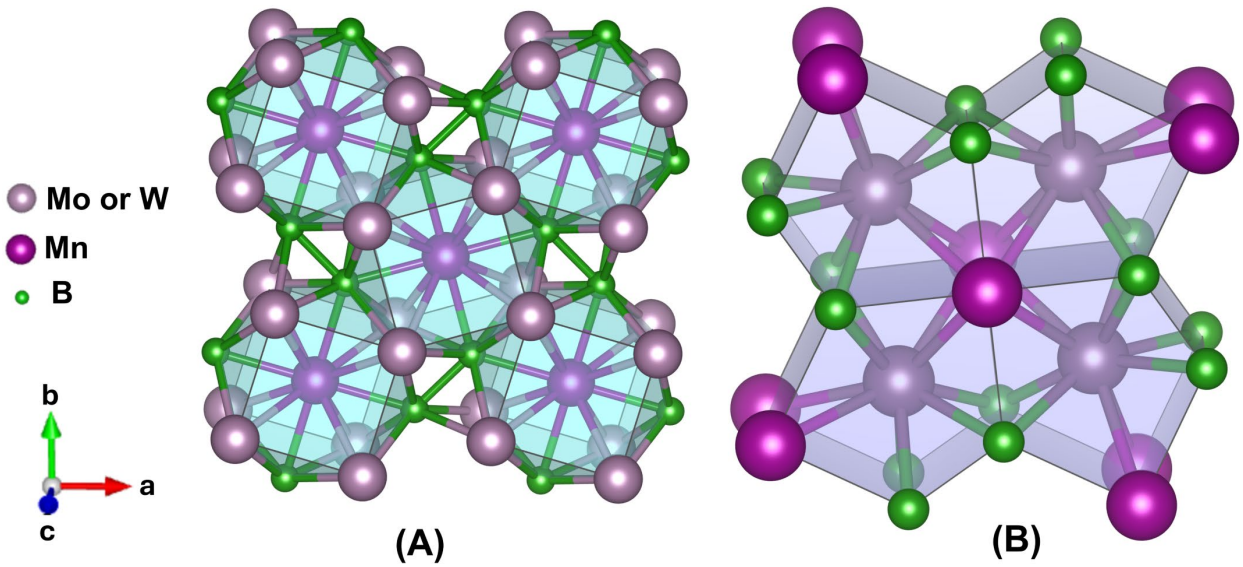


Figure 3. Coordination polyhedra structures. (A) Cuboctahedral coordination environment surrounding the Mn atoms, providing a stable bonding arrangement favored by their higher electron count. (B) Pentagonal prism coordination environment preferred by Mo or W atoms, consistent with their lower electron count. These distinct polyhedral environments reflect the electron-driven site preference and structural stability of the boride framework.

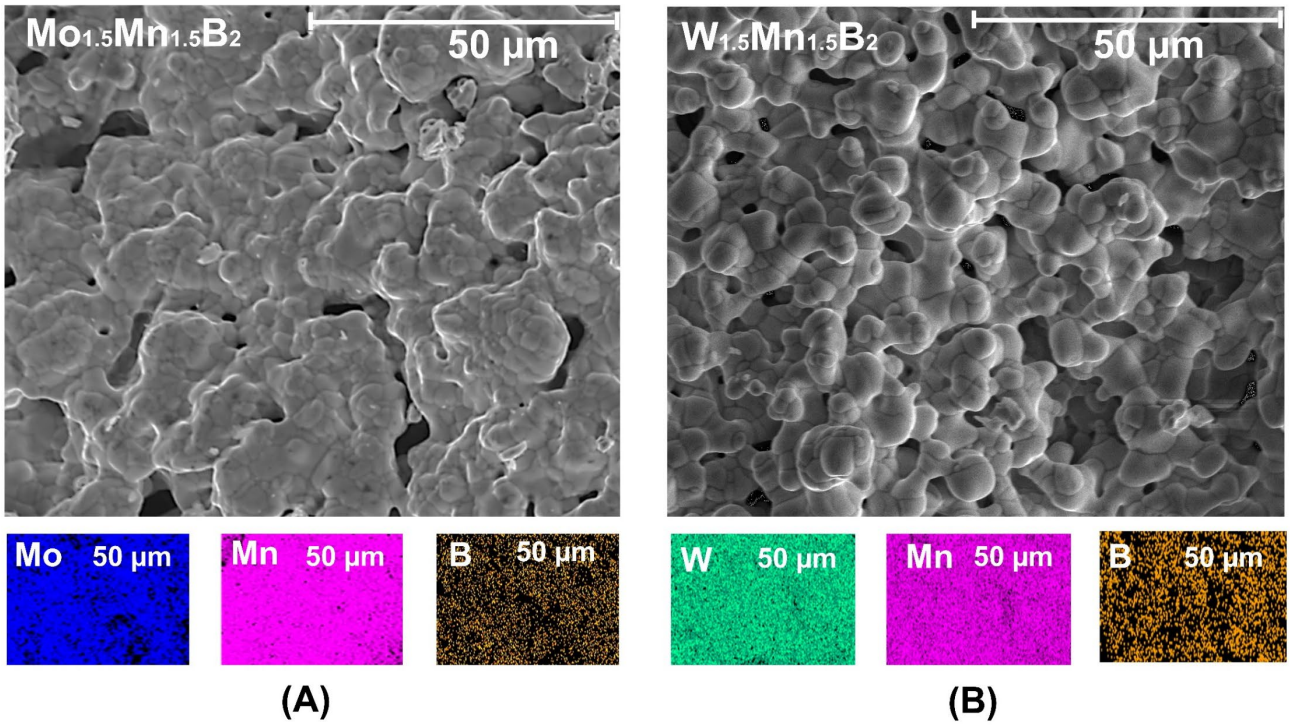


Figure 4. Scanning electron microscopy (SEM) images and corresponding energy-dispersive X-ray spectroscopy (EDS) elemental maps for $Mo_{1.5}Mn_{1.5}B_2$ (A) and $W_{1.5}Mn_{1.5}B_2$ (B). Both compounds exhibit homogeneous microstructures composed of uniformly shaped grey grains. Elemental mapping confirms the uniform distribution of Mo, Mn, and B in $Mo_{1.5}Mn_{1.5}B_2$, and W, Mn, and B in $W_{1.5}Mn_{1.5}B_2$, with no observable segregation or clustering, indicating excellent phase homogeneity.

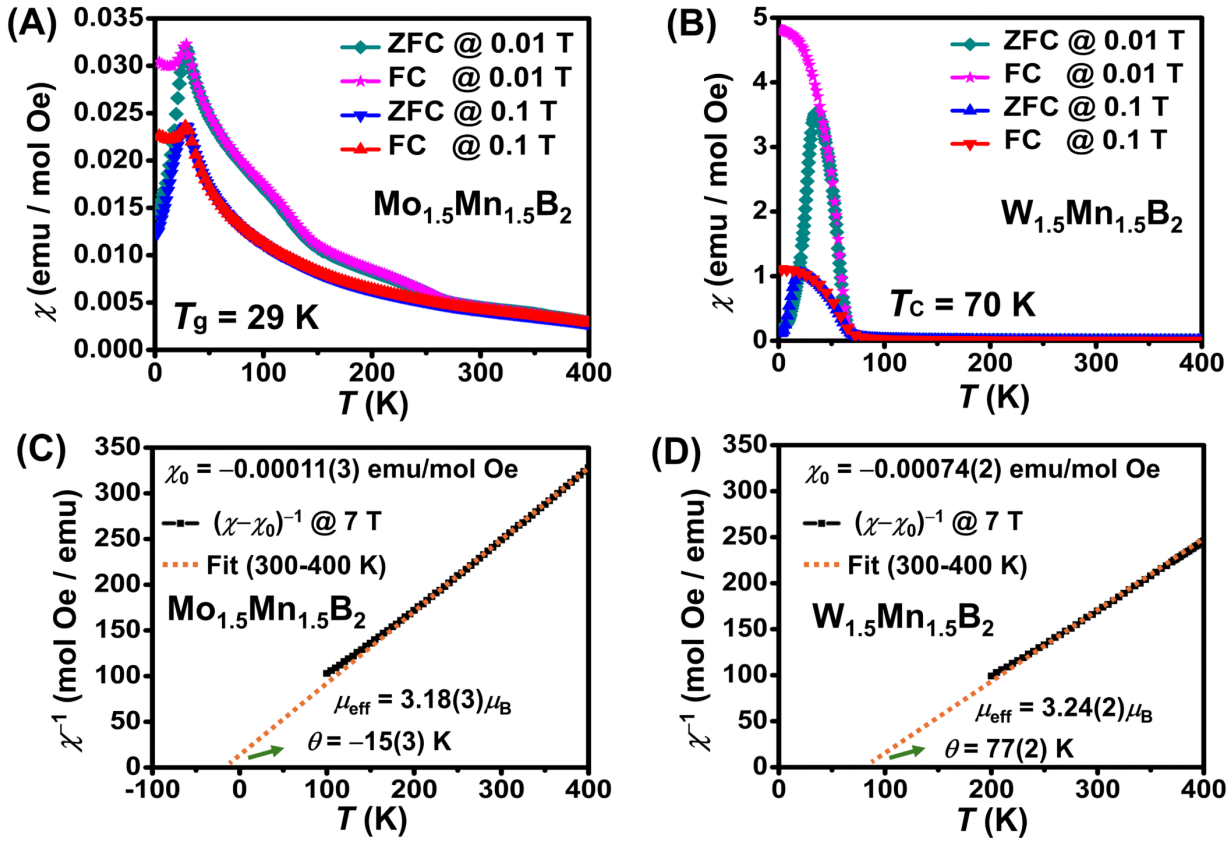


Figure 5. Temperature-dependent DC magnetic susceptibility (χ) and inverse susceptibility (χ^{-1}) for $Mo_{1.5}Mn_{1.5}B_2$ (A, C) and $W_{1.5}Mn_{1.5}B_2$ (B, D), measured under zero-field-cooled (ZFC) and field-cooled (FC) conditions. The freezing temperature is Tg = 29 K for $Mo_{1.5}Mn_{1.5}B_2$, while the Curie temperature is T_C = 70 K for $W_{1.5}Mn_{1.5}B_2$. C–D**:** High-field Curie–Weiss analysis at 7 T on the corrected inverse susceptibility $(\chi–\chi_0)^{-1}$, where χ_0 is a temperature-independent term (core diamagnetism plus a small Van Vleck contribution) measured under field-cooled (FC) condition. The orange dotted lines reflect the Curie-Weiss fits performed over 300–400 K. The analysis yields θ = –15 K for $Mo_{1.5}Mn_{1.5}B_2$ and a positive θ = 77 K for $W_{1.5}Mn_{1.5}B_2$.

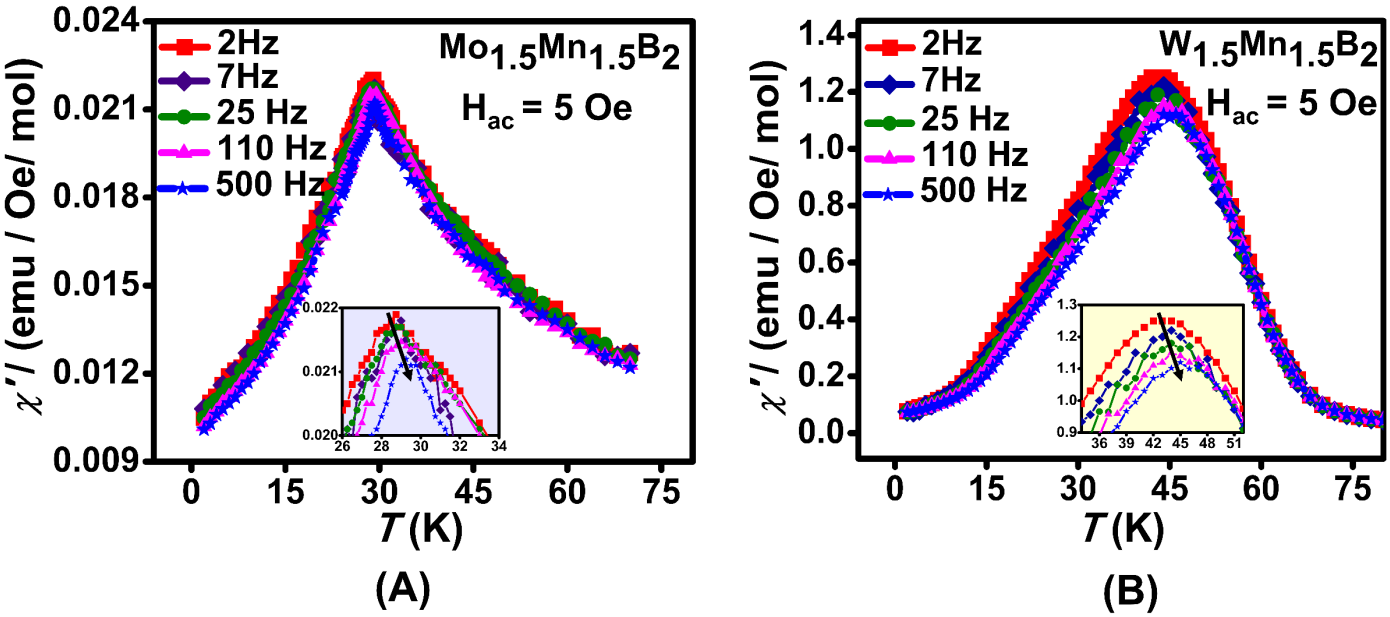


Figure 6. Real part of the AC magnetic susceptibility (χ') for $Mo_{1.5}Mn_{1.5}B_2$ (A) and $W_{1.5}Mn_{1.5}B_2$ (B), measured as a function of temperature at an AC field amplitude of H_{ac} = 5 Oe, DC applied field of H_{dc} = 100 Oe, and excitation frequencies of 2, 7, 25, 110, and 500 Hz. The peak in χ' shifts toward higher temperatures with increasing frequency in both compounds, consistent with thermally activated spin-glass dynamics. A sharper and more symmetric transition appears in $Mo_{1.5}Mn_{1.5}B_2$ near 30 K, while $W_{1.5}Mn_{1.5}B_2$ exhibits a much broader response near 43 K (just below T_C = 70 K), suggesting a re-entrant spin glass transition. Insets highlight the frequency-dependent shift of the freezing temperature, indicating distinct magnetic relaxation behavior between the two systems. The frequency dependence of T_f(f) was analyzed using the Power-law (critical slowing-down) and Vogel–Fulcher relations.

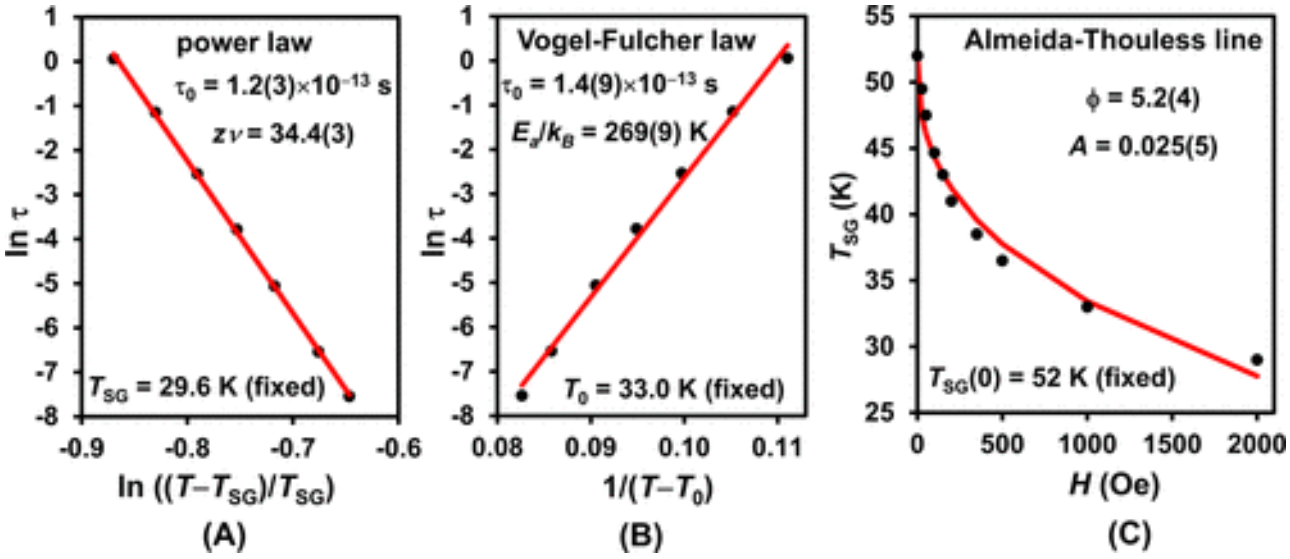


Figure 7. Dynamic AC-susceptibility analysis for $W_{1.5}Mn_{1.5}B_2$. (A) Power-law (critical slowing-down) fits to the frequency-dependent χ' peak positions, showing cooperative spin dynamics. (B) Vogel–Fulcher fit, yielding a finite interaction temperature T_0, consistent with interacting magnetic clusters. (C) Field dependence of the freezing temperature at fixed frequency (110 Hz): T_{SG} decreases with applied DC field following an Almeida–Thouless–type trend, indicative of non-mean-field glassiness. For all panels, black symbols are experimental values obtained from the χ'(T) maxima, and red lines are best fit to the indicated models.

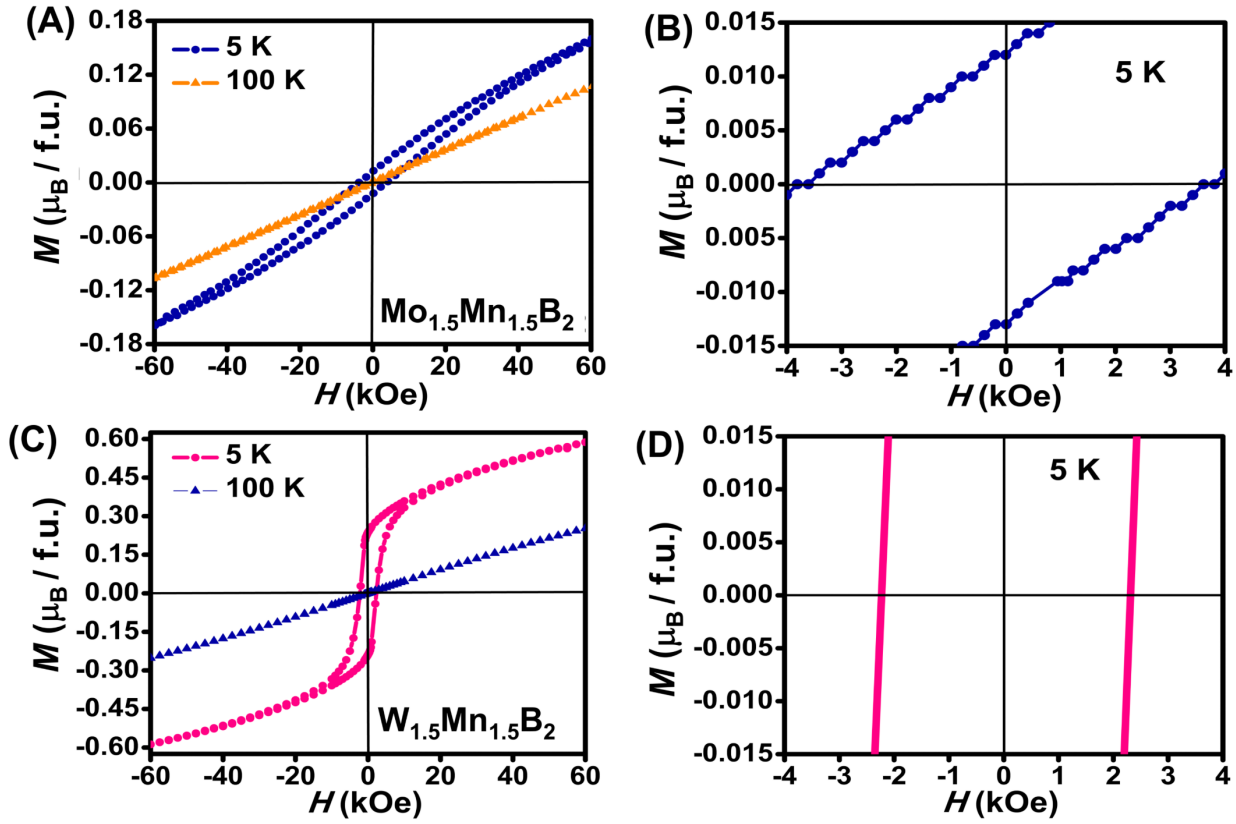


Figure 8. Field-dependent magnetization (*M*–*H*) curves for $Mo_{1.5}Mn_{1.5}B_2$ (A, B) and $W_{1.5}Mn_{1.5}B_2$ (C, D) measured at 5 K and 100 K. At 5 K, both compounds exhibit magnetic hysteresis characteristic of spin glass behavior for $Mo_{1.5}Mn_{1.5}B_2$ and weak ferromagnetic behavior for $W_{1.5}Mn_{1.5}B_2$. $Mo_{1.5}Mn_{1.5}B_2$ shows no sign of saturation, indicating a more pronounced spin-glass state, while $W_{1.5}Mn_{1.5}B_2$ tends to saturate, typical of a re-entrant spin-glass signature. At 100 K, the hysteresis vanishes for both compounds as they become paramagnetic. The zoom-outs (C, D) highlight the coercivity at 5 K, determined to be 3.80 kOe for $Mo_{1.5}Mn_{1.5}B_2$ and 2.20 kOe for $W_{1.5}Mn_{1.5}B_2$.

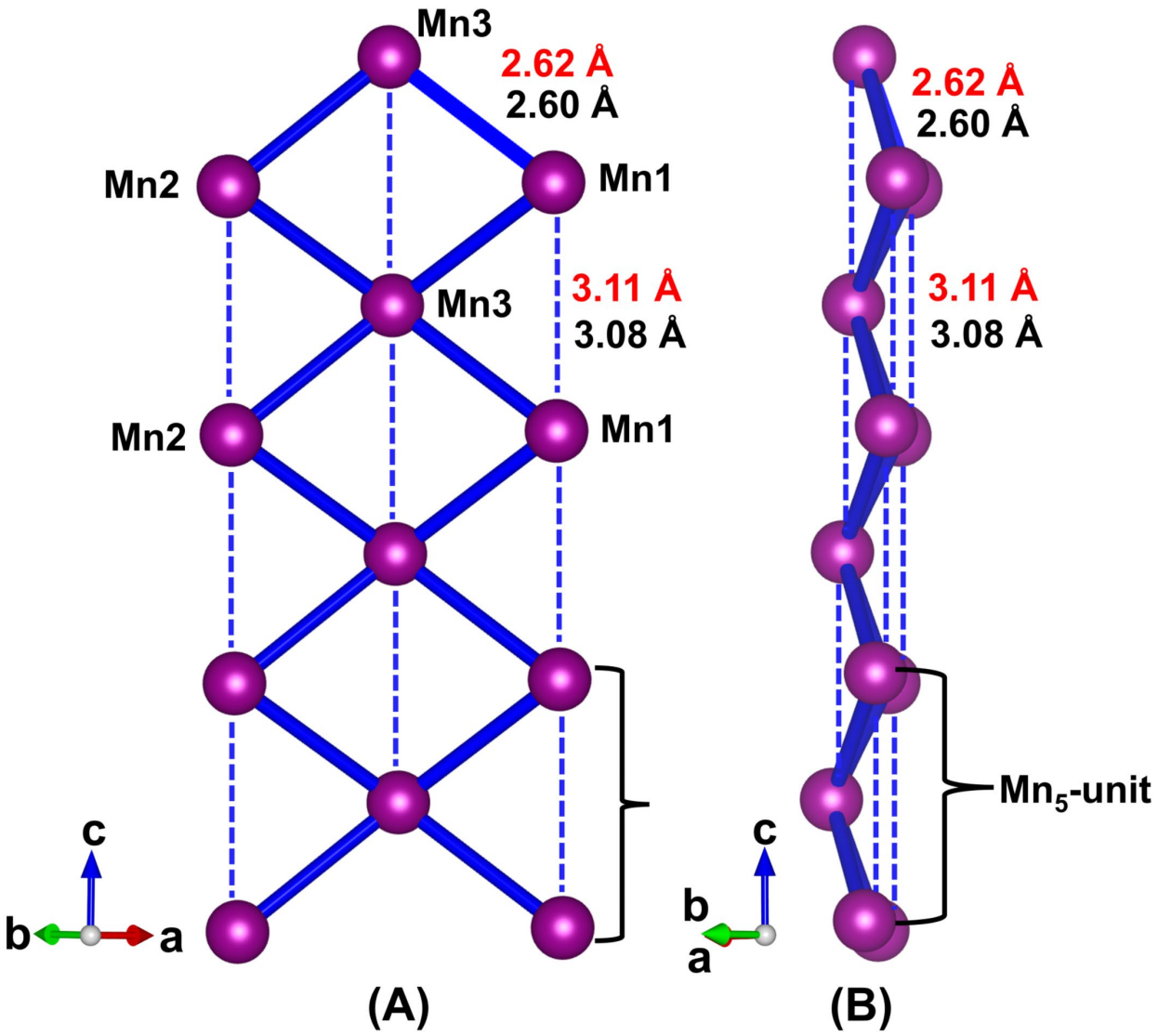


Figure 9. Magnetic Mn–Mn interactions building a unique chain of interconnected quadratic Mn_5-pyramids identified from the lowest-energy structural model of $wMo_{1.5}Mn_{1.5}B$ and $W_{1.5}Mn_{1.5}B_2$. The magnetic substructure in both compounds, viewed along different crystallographic axes, shows only a slight variation in Mn–Mn bond lengths: the bond length in $Mo_{1.5}Mn_{1.5}B_2$ (black) is marginally shorter than in $W_{1.5}Mn_{1.5}B_2$ (red). These Mn–Mn chains are vital in understanding the electronic and magnetic behaviors of these systems.

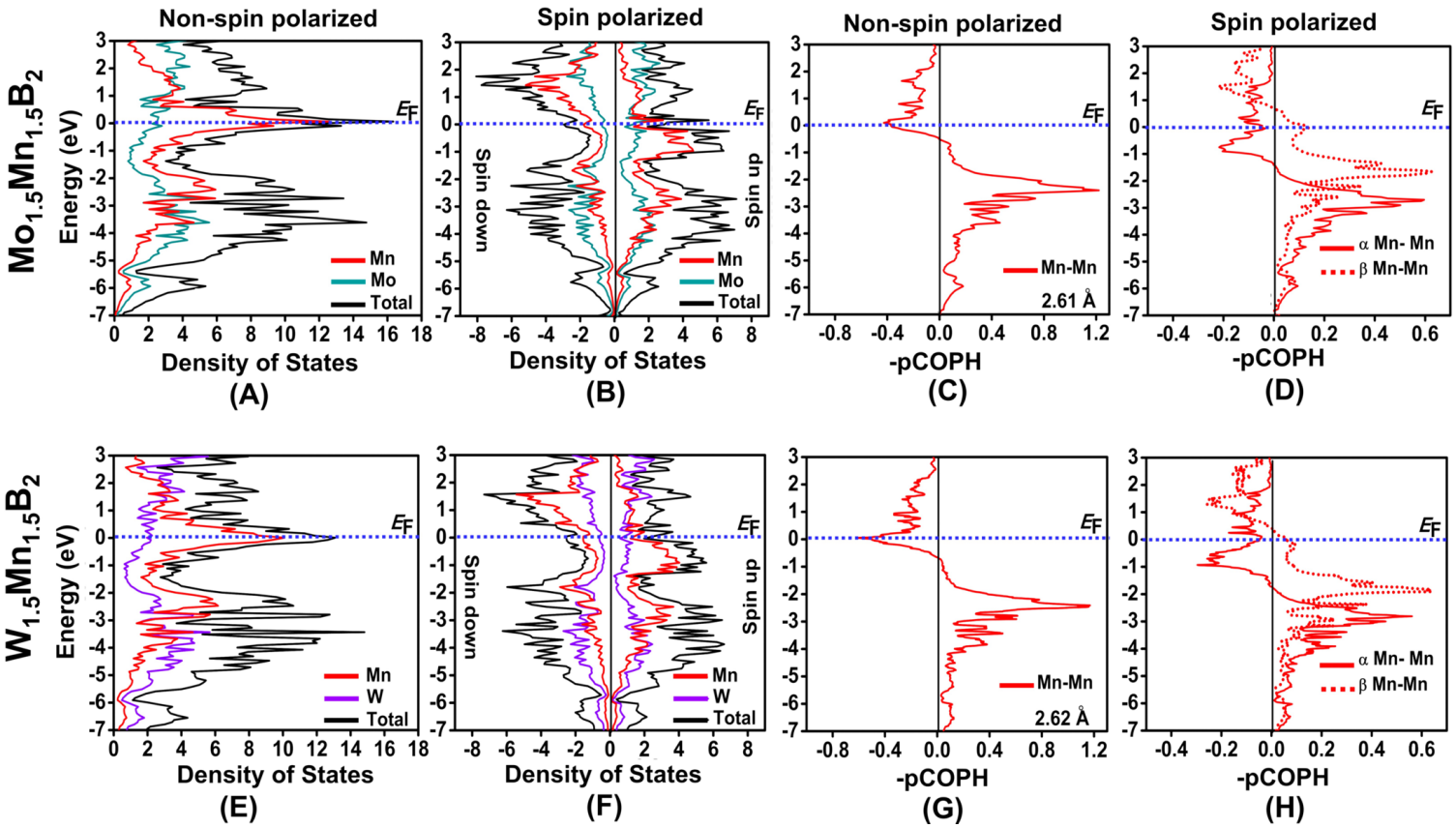


Figure 10. Electronic structure and bonding analysis of $Mo_{1.5}Mn_{1.5}B_2$ (A–D) and $W_{1.5}Mn_{1.5}B_2$ (E–H). (A, E) Non-spin-polarized total and partial density of states (DOS), indicating Mn 3d orbitals dominate near the Fermi level (E_F), confirming metallic behavior and Mn-governed magnetism. (B, F) Spin-polarized DOS with clear spin asymmetry, reflecting spin polarization effects. (C, G) Non-spin-polarized pCOHP curves for Mn–Mn interactions, showing the Fermi level resides in the antibonding region, suggesting instability in the nonmagnetic state. (D, H) Spin-resolved pCOHP separating α and β Mn–Mn interactions; the reduction of antibonding character and increase in bonding below E_F indicates stabilization via spin polarization.

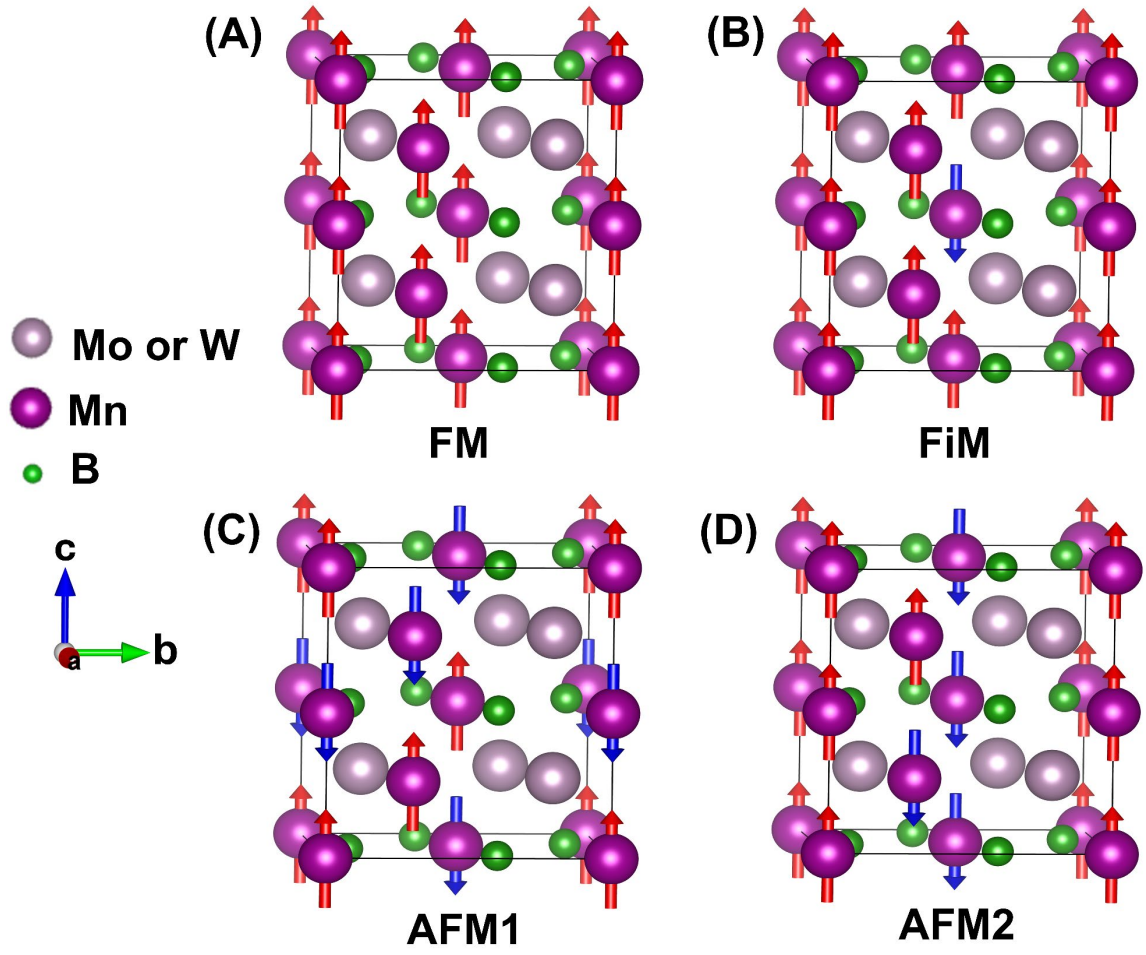
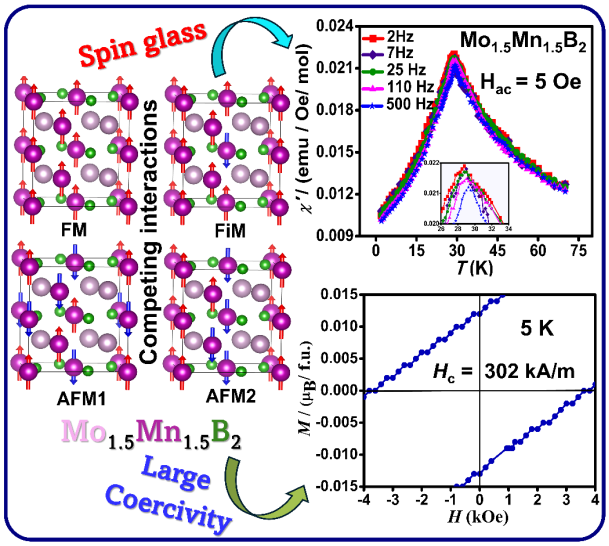


Figure 11. Magnetic configurations considered for $Mo_{1.5}Mn_{1.5}B_2$ and $W_{1.5}Mn_{1.5}B_2$: (A) ferromagnetic (FM), (B) ferrimagnetic (FiM), (C) antiferromagnetic type 1 (AFM1: antiparallel within Mn chains and between Mn layers), and (D) antiferromagnetic type 2 (AFM2: two parallel Mn chains aligned antiparallel to one another). Spin orientation is indicated by red (↑) and blue (↓) arrows. DFT calculations identify FM as the lowest-energy configuration in both compounds, with small energy differences relative to FiM and AFM models. The competition between these configurations suggests a complex magnetic landscape with potential for field-induced transitions.

TOC graphic



TOC Text

$M_{1.5}Mn_{1.5}B_2$ (M = Mo, W, Mo_2FeB_2-type, *P4/mbm*) were successfully synthesized as single-phase products and found to display unusual magnetic properties with spin-glass states accompanied by remarkably large coercivity values of 302.4 kA/m (M = Mn) and 175.1 kA/m (M = W). DFT calculations confirmed the presence of competing FM and AFM interactions and further revealed uniaxial magnetic anisotropy, thus confirming experimental findings.